UNIVERSITY OF CALIFORNIA SAN DIEGO

Enabling Low-Cost Cathodes in All-Solid-State Batteries

A Dissertation submitted in partial satisfaction of the requirements
for the degree Doctor of Philosophy

in

Materials Science & Engineering

by

Ashley Cronk

Committee in charge:

Professor Y. Shirley Meng, Chair
Professor H. Alicia Kim, Co-Chair
Professor Zheng Chen
Professor Ping Liu

2024

The Dissertation of Ashley Cronk is approved, and it is acceptable in quality and form for publication on microfilm and electronically.

University of California San Diego

2024

TABLE OF CONTENTS

LIST OF FIGURES

LIST OF TABLES

LIST OF ABBREVIATIONS

LIB	Lithium-ion battery
LFP	Lithium iron phosphate
SSE	Solid state electrolyte
ASSB	All-solid-state battery
Li-S	Lithium sulfur
EIS	Electrochemical impedance spectroscopy
SEM	Scanning electron microscopy
FIB	Focused ion beam
XRD	X-ray diffraction
TEM	Transmission electron microscopy
XPS	X-ray photoelectron microscopy
XAS	X-ray absorption spectroscopy
XANES	X-ray absorption near edge spectroscopy
FEM	Finite element method
LCO	Lithium cobalt oxide
NCM	Lithium nickel cobalt manganese oxide
NCA	Lithium nickel cobalt aluminum oxide

ACKNOWLEDGEMENTS

I first would like to acknowledge my family for their support. I would also like to acknowledge my faculty and research mentors at University of California, Berkeley, specifically Dr. Khalid Kadir, Dr. Francesca Toma, David Larson, Dev Mehta, and Dr. Paul Lum, for their mentorship and guidance. Through their support, I was granted opportunities to engage in research that was foundational for my graduate studies and future.

I would like to acknowledge Professor Y. Shirley Meng for her continued support and mentorship throughout my graduate education. Through her mentorship and guidance, I have grown both scientifically and professionally, which has truly shaped me to become a scientist that I am proud of.

Chapter 1 in full, is a reprint of the material as it appears in Overcoming the Interfacial Challenges of $LiFePO_4$ in Inorganic All-Solid-State Batteries. Cronk, Ashley; Chen, Yu-Ting; Deysher, Grayson; Ham, So-Yeon; Yang, Hedi; Ridley, Phillip; Sayahpour, Baharak; Nguyen, Long Hoang Bao; Oh, Jin An Sam; Jang, Jihyun; Tan, Darren H. S.; Meng, Y. Shirley, ACS Energy Letters, 2023. The dissertation author was the primary investigator and author of this paper.

Chapter 2, in full, has been submitted for publication and is currently under peer review. Cronk, Ashley; Wang, Xiaowei; Oh, Jin An Sam; Han, So-Yeon; Bai, Shuang; Ridley, Phillip; Chouchane, Mehdi; Huang, Chen-Jui; Cheng, Diyi; Deysher, Grayson; Yang, Hedi; Sayahpour, Baharak; Vicencio, Marta; Lee, Choonghyeon; Lee, Dongchan, Lee; Song, Min-Sang; Jang, Jihyun; Lee, Jeong Beom; Meng, Y. Shirley, Nature Energy, 2024, *Under Review*. The dissertation author was the primary investigator and author of this paper.

VITA

2019 Bachelor of Science in Civil Engineering, University of California Berkeley

2020 Master of Science in Materials Science & Engineering, University of California San Diego

2024 Doctor of Philosophy in Materials Science & Engineering, University of California San Diego

ABSTRACT OF THE DISSERTATION

Enabling Low-Cost Cathodes in All-Solid-State Batteries

by

Ashley Cronk

Doctor of Philosophy in Materials Science & Engineering

University of California San Diego, 2024

Professor Y. Shirley Meng, Chair
Professor H. Alicia Kim, Co-Chair

All-solid-state batteries (ASSBs) are one of the most promising systems to enable thermally resilient and high energy dense next-generation energy storage. While lithium-ion batteries (LIB) using layered oxide cathodes have made significant advancements, these cathodes are reaching their limits in terms of cost, capacity, and performance. This necessitates the development of cathode alternatives that are safer, high energy dense, and with lower cost, by reducing reliance on critical materials like cobalt and nickel. Pursuing cobalt- and nickel-free chemistries, like $LiFePO_4$ (LFP) and lithium-sulfur (Li-S) in ASSB architecture is a promising approach to solve some of the current limitations of LIBs. Replacing liquid electrolytes with non-

flammable solid-state electrolytes (SSE) can improve both safety and energy density. While SSEs offer many advantages, they often introduce interfacial challenges from resistive solid-solid contact, which can inhibit lithium transport necessary for practical operation. This poses new challenges for LFP and Li-S cathodes, requiring new design strategies due to their unique morphological and material properties.

The morphological features of LFP essential for improved electrochemical performance, are highlighted to elucidate the interfacial challenges when implemented in sulfide based ASSBs. For the first study, the compatibility of LFP with two types of solid-state electrolytes, Li_6PS_5Cl (LPSCl) and Li_2ZrCl_6 (LZC), are investigated. Irreversible redox products and interfacial degradation from LPSCl were found to be responsible for unstable performance. This work reveals the intrinsic incompatibility of LFP against sulfide-based SSEs. However, employing the chloride-based electrolyte, LZC, high-rate and stable cycling performance for over a thousand cycles is achieved at room temperature. Although LPSCl was found to be incompatible with LFP, it was found to facilitate beneficial properties when paired with Li-S cathodes. Li-S cathodes can realize some of the highest known energy densities. But similar to LFP, its development in ASSBs has been plagued by interfacial and (chemo)mechanical degradation. In the second study, a scalable synthesis method is introduced to overcome the challenges well known for solid-state Li-S batteries. Facilitating interfacial reactions between sulfur and LPSCl, optimizing the cathode/catholyte microstructure, and tuning the redox behavior of LPSCl was found to improve utilization and stability. As a result, this approach enables high loading sulfur cathodes up to 11 mAh cm^{-2} with stable operation at room temperature. Several high energy density cell architectures are also proposed and demonstrated. These studies establish new design principles for both LFP

and Li-S cathodes in ASSBs, potentially transforming the energy storage landscape by enabling safe, low-cost, and high energy dense storage solutions for a wide range of future applications.

Chapter 1 Overcoming the Interfacial Challenges of $LiFePO_4$ in Inorganic All-Solid-State Batteries

Introduction

After several decades of development, lithium-ion batteries have made monumental breakthroughs in both energy densities and cycle life. This has enabled their extensive market dominance in nearly all consumer devices and is now seeing extensive implementation in emerging applications, such as electric vehicles and stationary storage devices.[1,2] These performance improvements have been largely attributed to advancements in state-of-the-art commercial cathode materials, such as high-capacity lithium nickel cobalt manganese oxide (NCM) or nickel cobalt aluminum (NCA) cathodes, which are commonly used in electric vehicles or high voltage lithium cobalt oxide (LCO), commonly used in portable devices. However, the combined effects of rapidly growing demand, along with the limited availabilities and supply chain resource challenges of nickel (Ni) and cobalt (Co) mining have resulted in rising costs and shortages for these critical materials.[3] The problem, also exacerbated by the recent pandemic, has resulted in more than 430% and 125% increase in Ni and Co in prices per ton between 2020 and 2022.[4] While some believe this increase to be transient in nature leading to an eventual decrease, fundamental trends in sheer demand and limited supply of such critical materials have compelled manufacturers to explore cathode alternatives that overcome these supply and scarcity challenges. Next-generation energy storage systems should capitalize on low-cost abundant materials with reduced impact from supply chain fluctuations.[5] Thus, the lithium iron phosphate (LFP) cathode, first reported by Goodenough et al.[6] in 1997, has been extensively explored due to its negligible toxicity and high-rate capability. Recently, original equipment manufacturers have also announced plans for the adoption of LFP cathodes in their products, eliminating their reliance on conventional Ni- or Co- containing materials.[7,8] Furthermore, LFP-based chemistries are projected to account for 42% of the battery

demand by 2030 with the global demand expected to grow by thirteen times, exceeding 1 TWh by 2035.[9,10] Market outlooks coupled with the growing demand for electrified transport and grid storage, advocate for LFP to become one of the dominant cathode materials employed for most energy storage applications.

LFP exhibits an olivine crystal structure, facilitating one-dimensional lithium diffusion during (de)lithiation[11], where a two-phase reaction exists during the conversion of lithiated LFP to delithiated $FePO_4$.[12] Additionally, its strong P-O covalent bonds make LFP one of the safest commercialized cathodes.[11] LFP alleviates many of the safety concerns arising from conventional NCM or LCO type cathode materials that undergo thermal runaway at high temperatures.[13] However, safety hazards can still be present when using LFP, but only due to the commonly used highly flammable liquid organic electrolytes. Solid electrolytes can offer a safer alternative. Interestingly, research efforts on LFP in solid-state batteries have mainly utilized organic polymer electrolytes which can still exhibit some degree of flammability. Prior studies using LFP cathodes have mainly relied on polymer hybrid electrolytes or gel-type slurries.[14–26] While categorized as solid-state, polymer electrolytes still exhibit vital disadvantages such as their low ionic conductivities and the use of flammable organic additives. The low room temperature ionic conductivities of the solid polymer electrolytes are usually mitigated by high-temperature operation, which is a prevalent strategy used amongst prior works.[14,15,17,18,19,22,23,25,26] However, relying on high-temperature environments is not desirable for most energy storage applications. The use of oxidatively stable and conductive inorganic solid electrolytes that can enable the use of LFP at room temperature has yet to be reported.

Amongst the inorganic solid-state electrolytes (SSEs) previously investigated for ASSBs, argyrodite Li_6PS_5Cl (LPSCl) is a popular candidate due to its high room temperature ionic

conductivity (>1 mS cm^{-1}),[27] improved deformability (Young's Modulus of 30 GPa) compared to popular oxides, and dry room processing stability.[28,29] LPSCl possesses some drawbacks as well, such as poor interfacial stability due to its narrow electrochemical window[30], making cathode coatings a widely adopted strategy to mitigate LPSCl oxidation.[31] Despite having a low oxidation potential, LPSCl SSEs have been successfully paired against higher voltage (~4 V) cathodes like LCO or NMC, demonstrating the effectiveness of protective coating layers.[32–34] However, despite the lower operating voltage of LFP cathodes (3.5 V), there have been no studies to date on the compatibility of LFP against common inorganic SSEs such as LPSCl, with or without protective coating layers. Nonetheless, enabling cathodes in ASSBs without use of coating is still preferred. Therefore, SSEs with both favorable mechanical properties and improved electrochemical stability remains of interest to the field.

Recently, chloride-based SSEs have become an attractive candidate due to their high oxidation stability limits,[35] high room temperature ionic conductivities, along with favorable mechanical properties.[36,37] Early chloride SSEs reported include ternary compounds like Li_3YCl_6[38] and Li_3InCl_6[39] which, while oxidatively stable and highly conductive, still rely on costly elements. Various quaternary compositions have also been reported with the aim to increase ionic conductivity and reduce the use of expensive elements by creating disordered electrolyte structures.[40–42] A low-cost and earth-abundant alternative containing only zirconium, Li_2ZrCl_6 (LZC), exhibits comparable room temperature ionic conductivity with other reported chlorides ($0.4 - 0.8$ mS cm^{-1}).[40,43] Additionally, its relatively high oxidation potential of 4.5 V (vs. Li/Li^+) makes it a suitable material to compare to the commonly used sulfide-based LPSCl. Therefore, LZC was selected as the SSE candidate for our study with LFP cathodes.

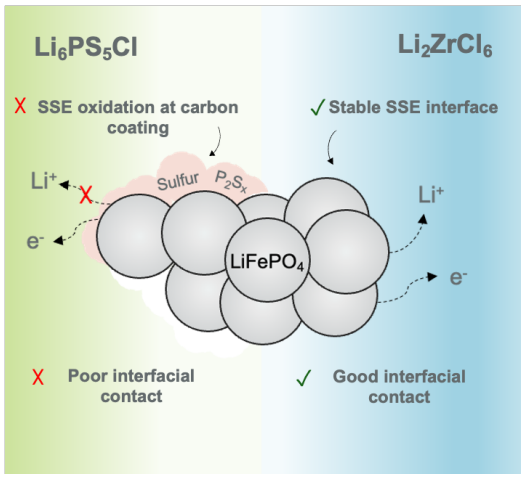

Figure 1.1: Schematic comparing the effects of the sulfide-based and chloride-based SSE candidates when used with LFP.

In this chapter, we report ASSBs capitalizing on a chloride-based LFP cathode composite, where no solvents, gel, or organic-based dispersant was used. We highlight the unique morphological and electrochemical properties of LFP, specifically its nanostructured features along with its carbon coating that requires the use of chloride-based SSEs to operate effectively. By investigating the interfacial stability of LFP cathodes against the commonly used sulfide-based electrolyte LPSCl, we demonstrate the intrinsic incompatibility of LFP against sulfide-based SSEs, despite the lower operating voltage of LFP compared to traditional NCM-type cathodes. This study provides insights into cathode composite design, especially when balancing the unique characteristics of cathode materials (i.e., morphology and SSE electrochemical stability) against a catholyte. The methodology used in this work connects SSE decomposition products to the impedance growth at the SSE/cathode interface. Ultimately, by capitalizing on the oxidatively stable LZC, high-rate capability at 2C and stable cycling (80% retention after 1000 cycles at 1C) was achieved at room temperature.

Results and Discussion

To verify the structural and electrochemical properties of LZC and LPSCl, X-ray diffraction was performed on the electrolytes for LZC (**Supplementary Figure 1.1a**) with Rietveld refinement for LPSCl (**Supplementary Figure 1.1b**). The conductivities of solid-state catholytes were measured and the resulting Nyquist plots are shown in **Supplementary Figure 1.1c**; LZC and LPSCl exhibit ionic conductivities of 0.7 and 1.3 mS cm^{-1}, respectively. Direct current polarization was conducted to determine the electronic conductivity (**Supplementary Figure 1.1d)** where LZC and LPSCl result in 8×10^{-9} S/cm and 1.6×10^{-8} S/cm, respectively. To highlight the drastic differences in electrolyte electrochemical stabilities, linear sweep voltammetry (LSV) was conducted to determine the electrochemical stability window (**Figure 1.2a)**. Oxidative sweeps to 5 V (vs. Li/Li^+) highlight the clear challenge of using LPSCl within the cathode composite, oxidation occurs near 2.3 V, where two oxidation peaks are observed at 2.3 V and 2.7 V, respectively. These results align well with the predicted oxidative decomposition of LPSCl to elemental sulfur, LiCl, and Li-P_2S_x species,[44] determined from first-principles calculations. To characterize electrolyte oxidation under comparable cell cycling conditions, specifically during the 0.1 mA cm^{-2} constant current charge to 4 V, electrolyte/carbon composite cathodes were used as the working electrode and LiIn as the counter electrode. During the charging process, significant capacity was obtained due to the decomposition of LPSCl, which began at 2.3 V (**Figure 1.2b**), aligning well with the electrochemical stability window measurements obtained in **Figure 1.2a**. A total charge capacity of 407.2 mAh g^{-1} was obtained, close to the theoretical capacity of 499.1 mAh g^{-1} for LPSCl.

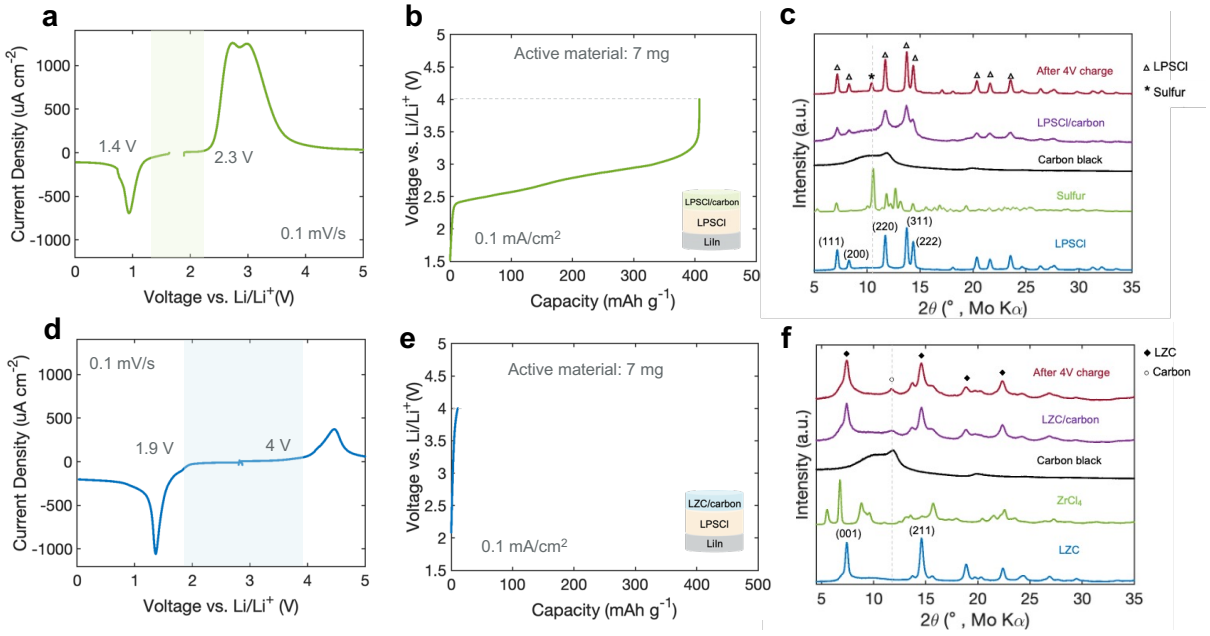

Figure 1.2: Linear sweep voltammetry, constant current charge behavior, and X-ray diffraction spectra of charged a), b), c) LPSCl and d), e), f) LZC where the shaded region in a) and d) represent the electrolyte stability window.

Post-mortem analysis was conducted on the charged electrolyte/carbon composites where bulk properties were determined by X-ray diffraction (XRD) (**Figure 1.2c and 1.2f**) and interfacial products detected with Raman spectroscopy (**Supplementary Figure 1.2)**. After the 4 V charge, elemental sulfur was detected in the XRD spectra where the main diffraction peak of (222) is observed at 10.53º 2θ (**Figure 1.2c**). The presence of elemental sulfur is further reinforced by the complementary Raman spectra, which displays peaks associated with vibrational modes evident of elemental sulfur at 154 cm^{-1}, 218 cm^{-1}, and 472 cm^{-1} as shown in **Supplementary Figure 1.2a**.

In contrast to LPSCl, the LZC oxidation sweep shows decomposition beginning at 4 V (**Figure 1.2d**) from the expected formation of Cl_2 (g) and $ZrCl_4$, while the reduction sweep to 0 V shows decomposition at 1.9 V attributed to the reduction of Zr^{4+} to metallic Zr. These results align well with LZC phase equilibria and first-principles calculations.[45] Further, LZC shows negligible

capacity contribution during the charge process as shown in **Figure 1.2e**, agreeing well with the obtained current density in the electrochemical stability window. XRD spectra of the charged LZC composite show no changes or evolution of new diffraction peaks observed after the 4 V charge (**Figure 1.2f**), reinforcing the oxidation stability of the chloride-based electrolyte. Rietveld refinement was conducted on the LZC/carbon composites where lattice parameters remained consistent after the 4 V (vs. Li/Li^+) charge as shown in **Supplementary 1.3.** No identifiable signature was detected on the Raman spectra of pristine and charged LZC (**Supplementary Figure 1.2b**), as vibrational peaks from LZC might exhibit low Raman activities which can be masked easily by the amorphous carbon. Overall, these results reinforce the disparities in electrolyte stability and capacity contributions between LPSCl and LZC. In addition, it also highlights the instability of LPSCl under oxidative conditions compared to LZC. The determined electrolyte stability windows reveal the lower oxidation stability of LPSCl, while LZC is highly stable up to 4 V, beyond the operating voltage of LFP, and is thus ideal as a solid-state electrolyte material for this system. Lastly, the post-mortem analysis results indicate that during the charged state, insulative oxidation products of LPSCl, mainly consisting of elemental sulfur, are generated and may hinder electrochemical performance including capacity utilization and cell polarization.

Beyond electrochemical stability, solid-state systems also require good contact between cathode and SSE solid particles to facilitate lithium-ion diffusion and to reduce interfacial resistance. Since the cathode active materials are constrained by the solid-state electrolyte, volume changes and internal pressure changes require compliant solid-state electrolytes. These critical interfaces within solid-state systems have previously been systematically reviewed,[46] where good electrolyte deformability was shown to be a key factor in addition to electrochemical stability and ionic conductivity. Sufficient deformability demands high densification under fabrication pressures,

creating minimal voids and better ionic connectivity throughout the cathode composite. To evaluate the densification properties of LZC and LPSCl, pellets were cold pressed under the typical cathode uniaxial fabrication pressure of 375 MPa, following procedures outlined in the experimental methods. After densification, *ex-situ* cross-section images were taken to evaluate the two-dimensional (2D) porosity.

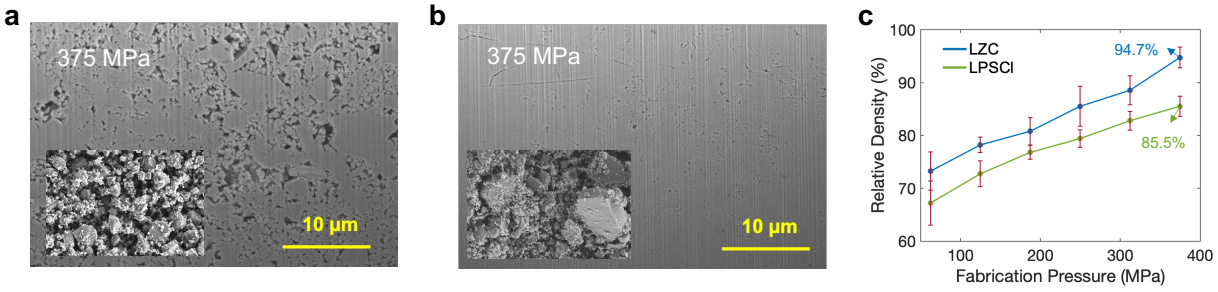

Figure 1.3: FIB cross-sections of cold-pressed pellets with inset showing SEM of particles at 10 µm scale of a) LPSCl and b) LZC. c) Relative density vs. fabrication pressure for LPSCl and LZC electrolytes.

For the LPSCl electrolyte, clear evidence of voids is present within the bulk (**Figure 1.3a**), compared to the LZC case which shows a highly dense surface (**Figure 1.3b**). 2D porosity was calculated using image binarization and pixel classification resulting in values of 14.5% and 3.7%, for LPSCl and LZC respectively, as shown in **Supplementary Figure 1.4**. SEM images of the loose powders were also obtained to investigate if particle size distribution had an effect. Interestingly, LPSCl possesses smaller particles, < 2 µm with a more uniform size distribution compared to LZC. We can see from the inset image in **Supplementary Figure 1.3b**, LZC exhibits

a wider particle size distribution (< 10 μm), which may assist in its improved densification properties compared to LPSCl.

Relative density versus fabrication pressure was also evaluated to compare electrolyte densification trends (**Figure 1.3c**). LZC achieves an overall higher relative density, where at the typical cathode fabrication pressure of 375 MPa, 94.7% density is attained, agreeing well with the 2D porosity calculations. Comparatively, LPSCl reaches 85.5% density which supports the 2D porosity calculation and prior work studying LPSCl densification and its relative density.[47] Focused ion beam (FIB) cross-sectional images and electron dispersive spectroscopy (EDS) mapping were also obtained for the LFP/SSE cathode composite in their pristine state (**Supplementary Figure 1.5**) where improved contact between the LFP particles and SSE was observed for the LZC case. In addition, the calculated porosity of 17% and 12% for LPSCl and LZC composites, reinforces the variance in mechanical and densification properties. These results suggest that the LZC electrolyte system enables better interfacial contact than LPSCl, an important feature when utilizing nanoscale cathode particles like LFP where surface contact is vital for good performance.

After establishing the oxidative stability and densification properties of both SSEs, cell-level electrochemical evaluation was conducted to observe how these varying properties affect electrochemical performance. The voltage profile for LFP/LPSCl cathode composite shows electrolyte oxidation during the first charge where a charge capacity of 114.3 mAh g^{-1} is obtained (**Figure 1.4a**) with a corresponding low discharge capacity of 46.1 mAh g^{-1}. Subsequent cycles are highly polarized with even lower LFP utilization. This is likely caused by impedance growth due to the formation of LPSCl oxidation products during the initial charge, which were shown to form beginning at 2.3 V, well before the LFP electrochemical reaction voltage. Approximately,

21.6% of this capacity is attributed to LPSCl oxidation, catalyzed by the high surface area carbon coated LFP. After oxidative decomposition products were formed, lithium transport is likely inhibited, which can explain the low initial Coulombic efficiency (ICE) of 40.3%. However, with the LZC catholyte, little to no electrolyte oxidation is observed during the first charge and very low polarization is observed in subsequent cycling. A higher charge capacity of 148.1 mAh g^{-1} and discharge capacity of 133.4 mAh g^{-1} is obtained with an ICE of 90.1% (**Figure 1.4b**). Similar ICE of 91.3% is obtained in a liquid electrolyte system (**Supplementary Figure 1.6c**) where an LFP electrode with a comparable areal capacity of 1 mAh cm^{-2} was evaluated to study the losses between the liquid and solid-state system. For more practical applications, a full cell using a silicon anode was assembled at the 3.5 mAh cm^{-2} level, where comparable capacities and ICE was obtained as shown in **Supplementary Figure 1.7**. This reinforces the stability of LZC and shows that with proper electrolyte selection similar performance to the liquid system can be achieved in ASSBs.

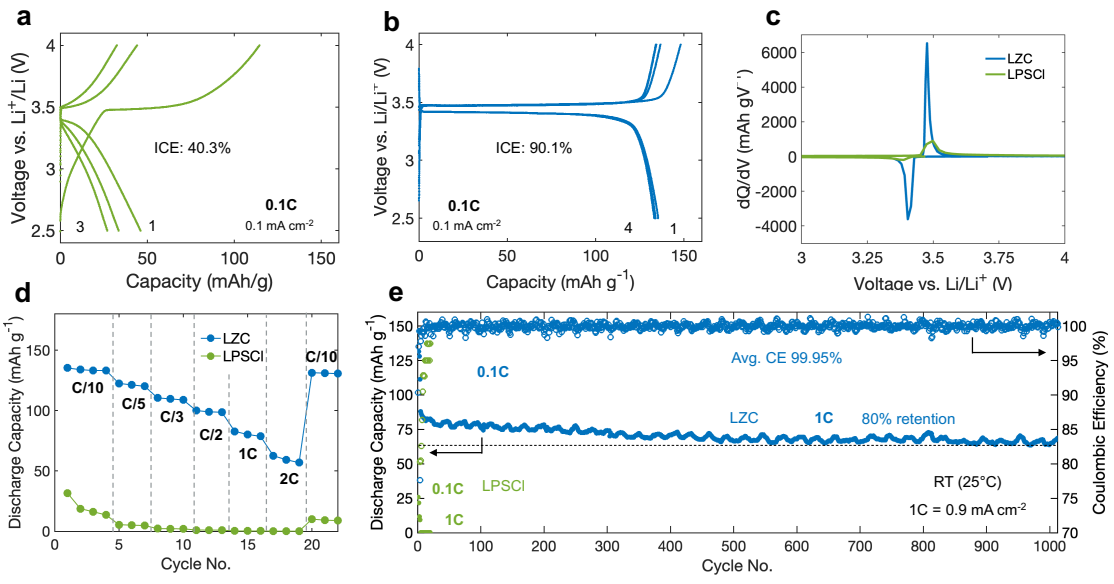

Figure 1.4: Electrochemical performance of LFP composite half cells. Voltage profiles at 0.1 mA cm^{-2} with a) LPSCl and b) LZC, c) Differential capacity plots of first cycle voltage profile, d) rate capability, and e) long-term cycling performance for LPSCl and LZC cells.

Differential capacity analysis was also conducted from the first cycle voltage profile of LPSCl and LZC (**Figure 1.4c**), where capacity is obtained using LPSCl before the two-phase LFP transition at 3.5V, another indication of electrolyte oxidation. Rate capability testing was conducted up to a rate of 2C where capacity of 65 mAh g^{-1} is attained with LZC, followed by a full discharge capacity recovery after returning to 0.1C (**Figure 1.4d**). Long-term cycling stability was also evaluated. Under 1C (0.9 mA cm^{-2}) cycling conditions, 80% capacity retention was obtained after 1000 cycles at room temperature (**Figure 1.4e**). A relatively low-capacity utilization is observed at higher C-rates, which is likely due to the lower room temperature ionic conductivity of LZC (~10^{-4} S cm^{-1}), inducing higher cell polarization for higher current densities. This can potentially be alleviated with the use of dopants to increase the ionic conductivity of the chloride SSE, which has been previously shown to increase ionic conductivities by up to an order of magnitude.[40–42] For the LPSCl case, little to no capacity is obtained under any elevated rate conditions due to the expected oxidation products and resulting impedance growth at the LFP/SSE interface. The continuous interfacial electrochemical reactions are further reinforced by the low coulombic efficiencies during cycling.

LFP particles are typically nano-sized and are coated in carbon as shown in **Supplementary Figure 1.6b**. While improvements in electronic conductivity was realized due to particle size reduction to the nanoscale, nanoparticles can pose significant interface challenges when paired with SSEs that exhibit poor electrochemical stability. This is due to the high surface area contact paired with the electronically conductive carbon that assists in the electrolyte oxidation, as discussed in prior works[48] and shown in **Figure 1.2** where large capacity was attained with LPSCl/carbon composites (**Figure 1.2c**). To evaluate how the amount of carbon coating

affects interfacial decomposition, elemental analysis was conducted to quantify the weight percentage of carbon at the surface of the LFP cathode where 1.6 wt.% of carbon was measured. Therefore, the total weight and volume percentage of coated carbon within the LFP/SSE composites used in this work is 0.62 wt.% and 0.78 vol.%, respectively. This means that < 1 wt.% and vol.% of carbon on the LFP particle surface can cause excessive decomposition when paired with LPSCl. For comparison, the volume percentage of the carbon additive VGCF within the cathode composite is much higher near 4 vol.%, highlighting how high surface area carbon coatings will accelerate the formation of decomposition products of SSEs unstable at the cathode operating voltage and further reinforcing the need for stable electrolytes to combat this challenge. These results also reinforce why LFP is less compatible with sulfide-based electrolytes versus other cathode materials like LCO or NMC, which are typically coated with electronically insulating layers and operate at higher charge voltages.

To characterize decomposition and local bonding environments on the cathode composite surface, X-ray photoelectron spectroscopy (XPS) was used to probe the LFP/SSE cathode composite at the charged state. The sulfur 2p spectra after the 4 V charge shows peaks which can be assigned to P_2S_x species and elemental sulfur (**Figure 1.5a**) based on previous work.[49] These results support the SSE oxidation products that were detected from the SSE/carbon composite post-mortem analysis in **Supplementary Figure 1.2**. Some P_2S_x species were also present in the pristine LFP/LPSCl composite, most likely attributed to chemical side reactions when in contact with the high surface area carbon-coated LFP. The phosphorus 2p region shows both PS_4^{3-} and P=O signatures in the pristine state attributed to LPSCl and LFP (**Figure 1.5b**). After charging, P_2S_x species are also detected in the P 2p spectra with additional phosphate species. Upon consecutive cycling, it would be anticipated that these insulative oxidation products would be

continually formed at the LFP/SSE and or carbon/SSE interface. For the LZC case, zirconium 3d (**Figure 1.5c**) and chlorine 2p (**Figure 1.4d**) spectra were collected where no changes in binding energies or evolution of new species were observed after charging. This further reinforces that the LFP/LZC cathode composite experienced little to no oxidation under these conditions.

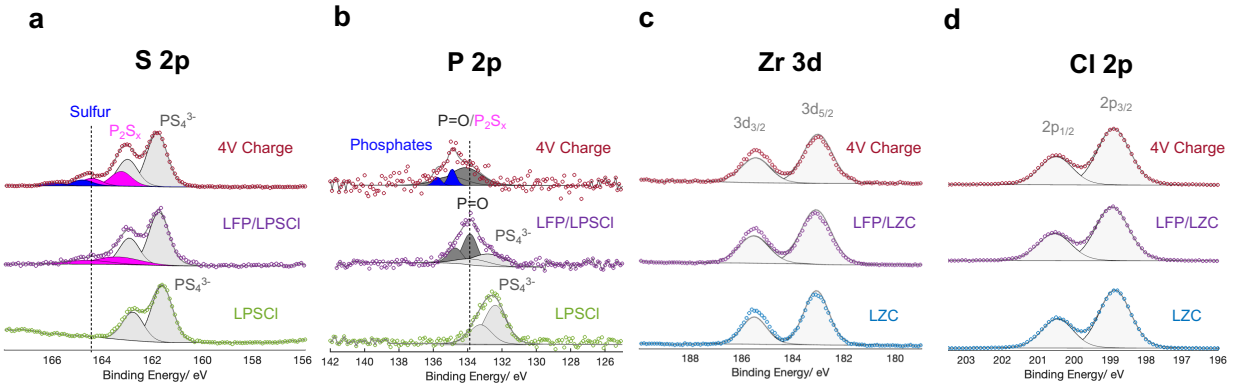

Figure 1.5: a) S 2p and b) P 2p XPS spectra for LPSCl, pristine composite, and after 4 V charge. c) Zr 3d and d) Cl 2p XPS spectra for LZC, pristine composite, and after 4 V charge.

The bulk properties of these charged cathode composites were also analyzed at various degrees of de-lithiation. XRD patterns of the LPSCl composite after the 4 V charge show little evidence of the $FePO_4$ (FP) phase (**Supplementary Figure 1.8a**) while the LZC composite shows signs of the expected FP phases formed (**Supplementary Figure 1.8c**). Undetectability of the FP phase supports the low-capacity utilization percentage of 65.4% with LPSCl. It should be noted that a percentage of this capacity is attributed to SSE oxidation and not necessarily de-lithiation of the cathode. Detectability of the FP phase within the bulk cathode composite reinforces the capacity utilization percentage of 83.7% with LZC. In addition, Raman spectra also reinforce these findings where peaks attributed to FP vibrational modes are present for the LZC case at 189 cm^{-1}, 305 cm^{-1}, and 335 cm^{-1} (**Supplementary Figure 1.8d**), as assigned in prior work.[50] Bulk properties of the LPSCl cathode composite in the charged state reveal that electrolyte oxidation

inhibits lithium transport during de-lithiation. LFP particle volume change of ~6.0%[51] and the poor densification of LPSCl can cause additional void formation leading to reduced interfacial contact. Any intimate interface further degrades when interfacial oxidation products like sulfur and phosphorus sulfides are generated as confirmed by XPS.

After oxidation products were confirmed and identified, electrochemical impedance spectroscopy (EIS) was conducted to quantify the impedance growth within the cathode composite during cycling. With the LFP/LPSCl composite, EIS was conducted after the first and third cycle where the capacity appears to have stabilized, and the data were fitted using the following equivalent circuit shown in **Figure 1.6a**. The high-frequency region can be assigned to the bulk SSE resistance. The intermediate frequency range is attributed to the cathode electrolyte interface (CEI) and the low-frequency region is assigned to the charge transfer (CT) resistance.[52] Fitting results shown in **Figure 1.6b**, show resistance contributions where after the first cycle, 96 Ω is assigned to the CEI growth and 505 Ω is assigned to CT. After the third cycle, we observe a large growth in both CEI and CT, confirming that with subsequent cycling, LPSCl oxidation products and poor interfacial contact caused by a porous composite lead to large impedance growth even just after the third cycle. This supports the electrochemical performance results, where for the third cycle, a low discharge capacity of 27 mAh g^{-1} is obtained (**Figure 1.4a**).

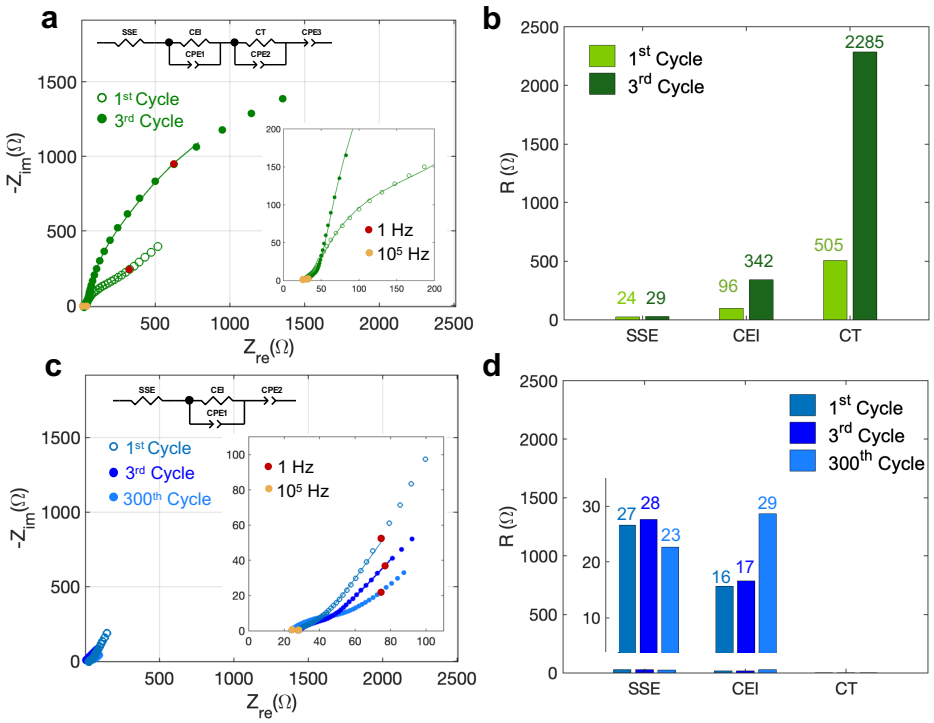

Figure 1.6: Nyquist plots and equivalent circuit fitting results from electrochemical impedance spectroscopy measurements for a-b) LPSCl and c-d) LZC.

With the LFP/LZC cathode, EIS was conducted after the 1st, 3rd, and 300th cycle, showing that impedance growth after extended cycling grows marginally. EIS results were fitted to the following circuit shown in **Figure 1.6c**, where the high-frequency range is attributed to the bulk SSE resistance and intermediate frequency region is assigned to the CEI. The bulk SSE resistance is higher for the LZC composite than the LPSCl, since LPSCl exhibits higher ionic conductivity. Fitting results shown in **Figure 1.6d** show that after the first cycle, CEI resistance is 16 Ω with marginal growth after 300 cycles to 29 Ω. Even after 300 cycles, the CEI resistance of the LFP/LZC composite is less than LFP/LPSCl even after the first cycle. The complete EIS fitting results for both composites are shown in **Supplementary Table 1.1**. Quantifying the impedance of the cathode composites after cycling confirm the hypothesis that for the LPSCl case, oxidation products are generated after the first charge. These oxidation products inhibit lithium-ion transport

leading to large impedance growth, attributed to CEI growth during subsequent cycling. Due to the high oxidative stability of LZC and good interfacial contact, impedance growth with extended cycling is negligible, leading to an improved electrochemical performance at high rates.

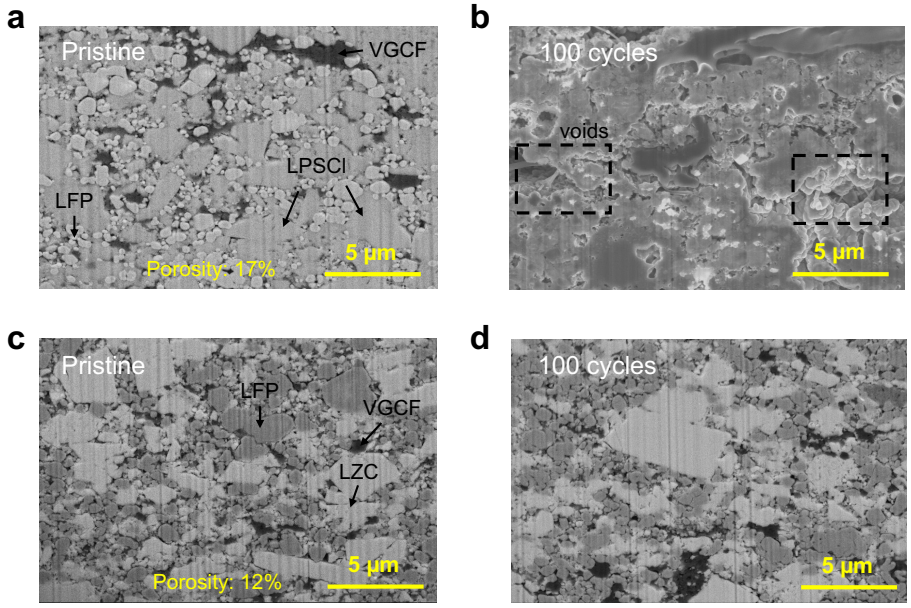

Figure 1.7: FIB-SEM cross sections of pristine and cycled LFP/SSE composites with a), b) LPSCl and c), d) LZC electrolytes at the discharged state.

To analyze interfacial degradation and morphology, FIB cross-sections were obtained of the post-cycled LFP/SSE cathode composites as shown in **Figure 1.7**. Compared to the pristine LFP/LPSCl composite (**Figure 1.7a**), its cycled counterpart (**Figure 1.7b**) displays clear evidence of voids and poor interfacial contact likely attributed to the formation of interfacial decomposition products, LFP volume change, and the poor densification of LPSCl. Since the solid-state system is physically constrained, expansion and contraction of the cathode particles cause internal stresses on the solid electrolyte. If the solid electrolyte exhibits reduced deformability, like LPSCl compared to LZC, as shown in **Figure 1.3**, intimate contact will degrade with consecutive cycling. These results help explain the large impedance growth and electrochemical performance with LPSCl. However, with

the LFP/LZC composite, morphology and interfacial contact are well preserved after 100 cycles (**Figure 1.7c and 1.7d**), and even after the charged state (**Supplementary Figure 1.9**) where no clear changes are observed. Preservation of the LFP/LZC interface assists in elucidating the improved electrochemical performance and marginal impedance growth with cycling.

In this work, sulfide and chloride solid electrolytes were investigated to elucidate the critical interfacial challenges of nanoscale carbon-coated LFP in ASSBs. With the sulfide-based LPSCl, poor oxidative stability and incompatibility with high surface area carbon-coated LFP caused excessive electrolyte oxidation forming elemental sulfur and phosphorus sulfides which inhibited lithium transport and led to large impedance growth during cycling. This resulted in poor electrochemical performance and shed light on why numerous prior works on solid-state LFP chemistries required the use of polymers or liquid additives. In contrast, with the chloride-based LZC, high oxidative stability and mechanical deformability facilitated a stable and passivating interface and good interfacial contact, resulting in marginal impedance growth with subsequent cycling. The stable interface between LFP and LZC enabled extended cycling performance of 1000 cycles (80% retention) at 1C without requiring elevated temperature conditions. These results showcase the importance of interfacial cathode composite design for high-performance ASSBs and highlight the need to consider the cathode's morphological surface as well as electrochemical properties in future SSE selection methodology.

Supplementary Information

Material Synthesis and electrode fabrication. Materials were dried under vacuum at 80ºC if not anhydrous and stored under inert conditions in an argon-filled glovebox. The sulfide solid-state electrolyte separator layer used in the Li-ASSB system is LPSCl for its relatively high conductivity

(around 3 mS cm^{-1} at room temperature) purchased from NEI Corporation. LZC was synthesized using procedures discussed in prior work.[40,45] Successful synthesis of LZC was confirmed via XRD as shown in **Supplementary Figure 1.1**. For electrochemical evaluation, the cathode composite consists of LFP powder (KJ2, China) (**Supplementary Figure 1.5a** and **Supplementary Figure 1.5b**), vapor grown carbon fiber (Sigma Aldrich, USA) and solid-state electrolytes are mixed in a mortar and pestle until homogenous. For the sulfide case, LPSCl was wet milled following the optimized procedure discussed in prior work[53] to reduce the particle size. For the chloride case, LZC was used directly after synthesis. LFP cathode composites were constructed in 40:57:3 wt.% ratios with an approximate loading of 1 mAh cm^{-2}. For electrochemical stability measurements, the cathode composite contained 70:30 wt.% of solid-electrolyte and carbon black, which was milled using a planetary ball mill for 1 hour at 300 rpm. This was done to ensure sufficient contact points between the electrolyte and electrode, facilitating a more accurate measurement versus planar electrode configurations.

Electrochemical Measurements. Electrochemical measurements were performed in custom pellet cells constructed of 10 mm Grade 5 titanium plungers and polyether ether ketone (PEEK) dies. For cell evaluation and LSV measurements, the cathode and separator layers are pressed to 3 tons (375 MPa), while the $Li_{0.5}In$ or Li metal anode is pressed to 1 ton (125 MPa) or 0.2 ton (25 MPa), respectively. For EIS and DCP measurements, the separator layer is pressed to 3 tons and carbon black is added to both sides to ensure sufficient contact. After assembly, the pellet cells are inserted into custom cell holders and hand tightened to 70 MPa. EIS, DCP, and LSV measurements were collected using a Solartron 1260 instrument. For EIS measurements, an applied voltage amplitude of 30mV and frequency range of 7 MHz to 20 mHz was used. For DCP measurements, the applied voltage range was 100 to 800 mV, where a linear fit was used to determine the electrical resistance.

For LSV measurements, a sweeping rate of 0.1 mV/s was used to both OCV to 5 V and OCV to 0 V. Ionic conductivity of materials was determined using the following equation $\sigma = \frac{L}{RA}$, where L is pellet thickness, R is resistance, and A is the area of the pellet cell (10 mm = 0.785 cm^2). Electronic conductivity was calculated using Ohm's law, where $R = \frac{V}{I}$, and is obtained from the current response while applying a voltage which is substituted in the above conductivity equation. For electrochemical performance evaluation, cells were cycled under 50 MPa at room temperature with $Li_{0.5}In$ acting as the counter electrode. Capacity utilization and cell cycling was evaluated using Landt Instrument cyclers (CT3001A).

Surface Characterizations. Scanning electron microscopy (SEM) was performed on a FEI Apreo and/or FEI Scios DualBeam focused ion beam (FIB)/SEM with 5 kV accelerating voltage and 0.1 nA beam current for powders and pellets. Powder and pellet samples were prepared in an argon-filled glovebox and transferred using a transfer arm to avoid any air exposure. For the FIB cross-section, Ga was used as an ion beam source. Parameters used for all milling conditions of 30 kV, 65 nA, with the subsequent cross-section cleaning performed with 30 kV, 15 nA. Raman spectra were acquired with a Renishaw inVia upright microscope using 532 nm source (10% laser power) and 25× objective. Powder samples were prepared in an argon-filled glovebox.

X-ray Diffraction. XRD measurements were collected by a Bruker SMART instrument using Mo K_α (λ = 0.71 Å) radiation and a Platinum 135 CCD detector at the UCSD X-Ray Crystallography Department. The measurements were performed from 5 to 90° 2θ and collected at ambient temperature. Samples were prepared in an argon-filled glovebox using 0.7 mm boron capillaries,

and flame sealed to ensure air-tight measurements of sensitive samples. Rietveld refinement analysis was performed using GSAS-II software.[54]

Elemental Analysis: Elemental analysis was performed on a Perkin Elmer PE2400-Series II, CHNS/O analyzer. Samples were dried under in argon under vacuum for 10 hours at 150°C prior to measurements.

X-ray Photoelectron Spectroscopy. XPS measurements were conducted using a Kratos Axis Supra XPS instrument. Al Kα radiation was used, with a chamber pressure of less than 5×10^{-8} torr during operation. A charge neutralizer was used for insulating samples and the scan resolution was 0.1 eV with a dwell time of 100 ms. CasaXPS was used for fitting and analysis.[55] The data was calibrated based on the C 1s peak at 285 eV where a Shirley-type background was used.

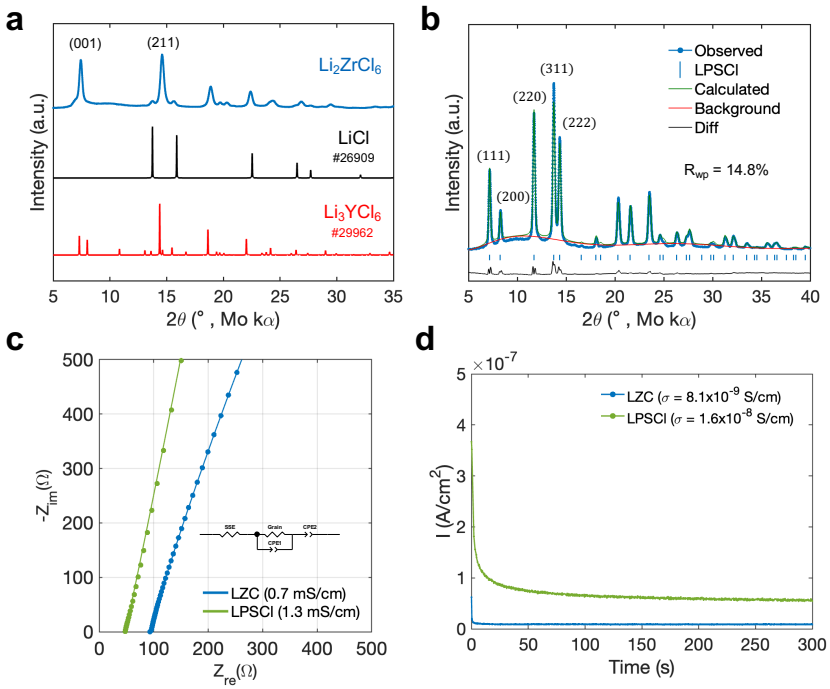

Supplemental Figure 1.1: Properties of solid-state electrolytes. a) XRD of LZC plotted against LiCl and Li_3YCl_6 with representative parent crystal structure, b) Rietveld refinement result of LPSCl c) Nyquist plot of EIS results, and d) DC polarization measurements

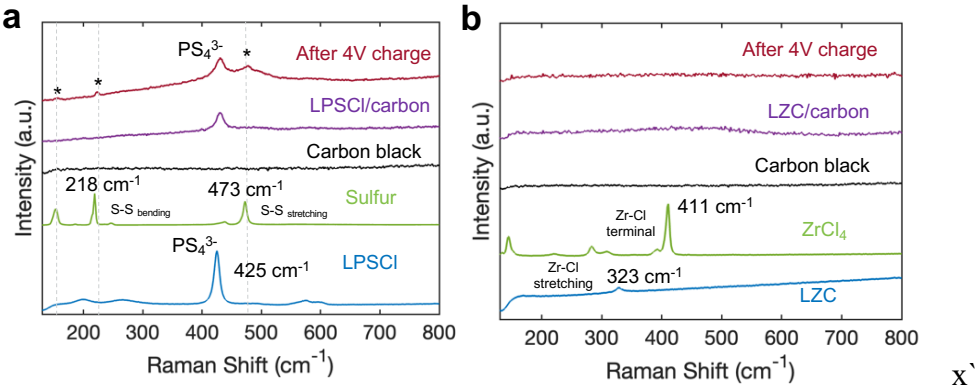

x`

Supplemental Figure 1.2: Raman spectra of charged carbon/SSE half cells a-b) LPSCl and c-d) LZC.

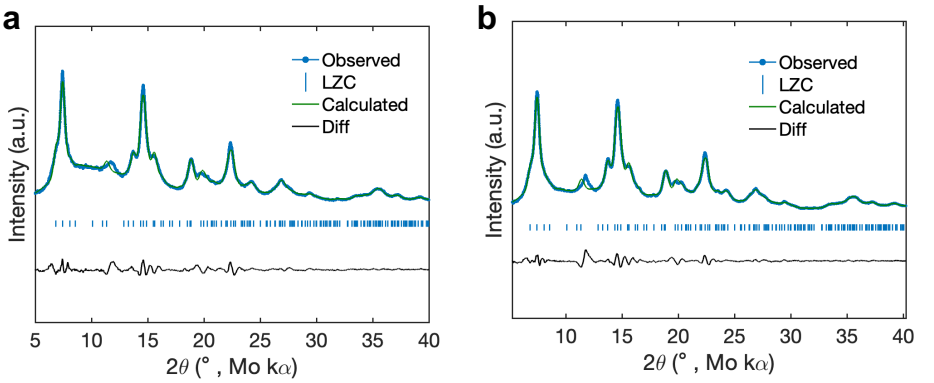

LZC pristine	a	b	c	γ
	10.95 Å	10.95 Å	5.936 Å	120°

LZC charged	a	b	c	γ
	10.93 Å	10.93 Å	5.936 Å	120°

Supplemental Figure 1.3: Rietveld refinement of a) pristine LZC/carbon composite and b) charged LZC/carbon composites with lattice parameters.

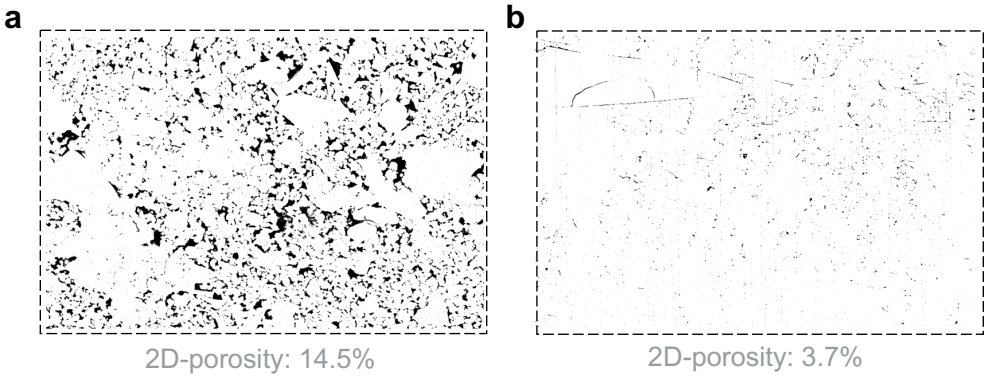

Supplemental Figure 1.4: Binarized FIB cross-section image of cold-pressed SSE pellets where voids are assigned to black pixels a) LPSCl and b) LZC with calculated 2D-porosity.

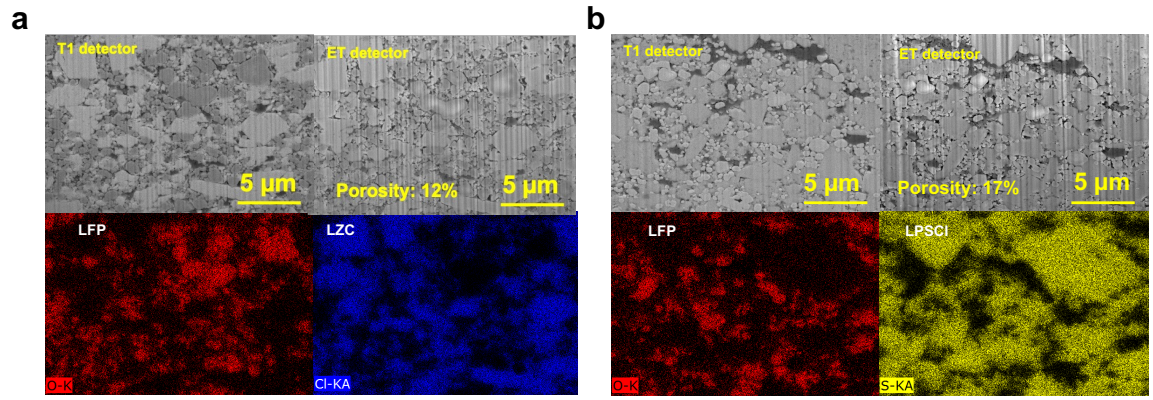

Supplemental Figure 1.5: Focused ion beam (FIB) cross-sections and electron dispersive spectroscopy (EDS) mapping of pristine LFP composite with a) LZC and b) LPSCl solid-state electrolytes

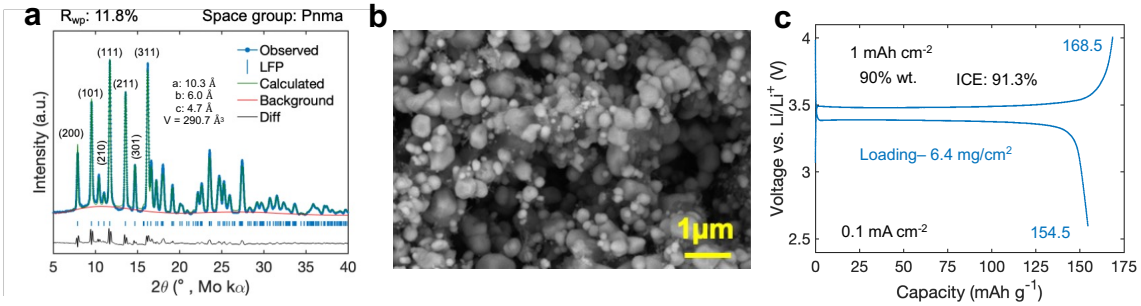

Supplemental Figure 1.6: Characterization of LFP cathode materials. a) Rietveld refinement result, b) SEM of LFP powder and c) liquid cell performance in LFP/Li metal half cells.

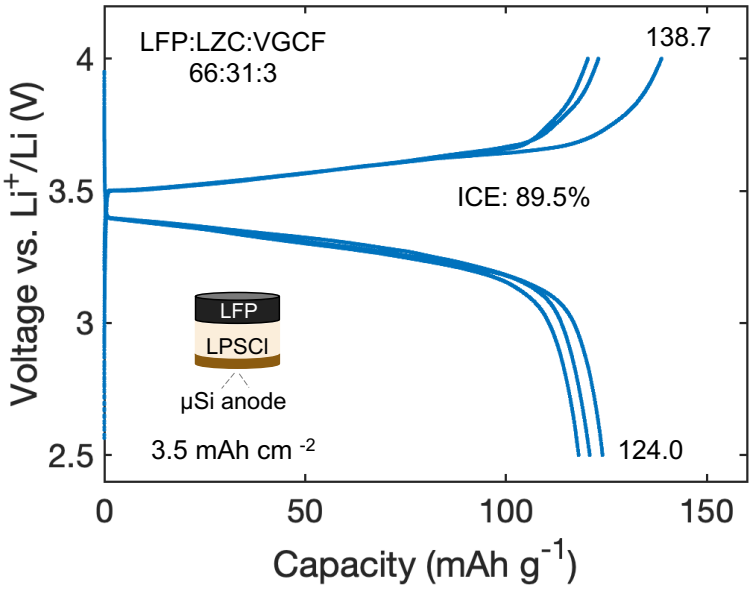

Supplemental Figure 1.7: Full cell demonstration using a silicon anode with 66 wt. % LFP at the 3.5 mAh cm^{-2} level.

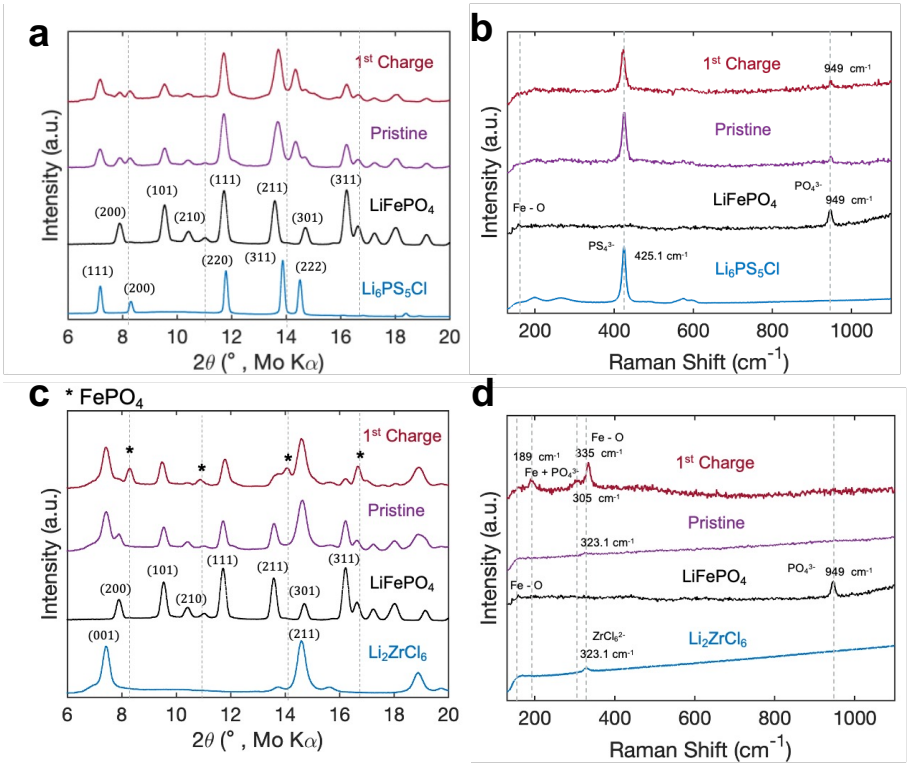

Supplemental Figure 1.8: XRD and Raman of cathode composites in the charged state using LPSCl (a-b) and LZC (c-d).

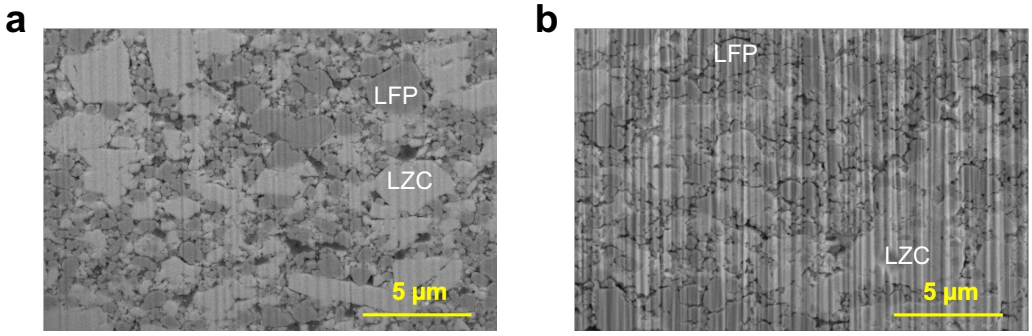

Supplemental Figure 1.9: FIB cross-sections of a) pristine and b) charged LFP composites with LZC electrolyte.

Supplemental Table 1.1: EIS fitting results of LFP composite half cells after 1st, 3rd, and every 100th cycle for LZC.

Composite	Cycle	Resistance (Ω)			Capacitance (10^{-3} F)		$\chi^2(10^{-3})$
		SSE/Bulk	CEI	CT	CEI	CT	
LFP/LPSCl	1st	24	96	505	0.2	0.7	1.4
LFP/LZC	3rd	29	342	2285	0.1	0.1	0.7
	1st	27	16	0	3.9	/	2.0
	3rd	28	17	0	2.1	/	0.4
	100th	26	19	0	2.0	/	0.8
	200th	22	20	0	2.0	/	2.3
	300th	23	29	0	1.9	/	3.0

Acknowledgements

Chapter 1 in full, is a reprint of the material as it appears in Overcoming the Interfacial Challenges of $LiFePO_4$ in Inorganic All-Solid-State Batteries. Cronk, Ashley; Chen, Yu-Ting; Deysher, Grayson; Ham, So-Yeon; Yang, Hedi; Ridley, Phillip; Sayahpour, Baharak; Nguyen, Long Hoang Bao; Oh, Jin An Sam; Jang, Jihyun; Tan, Darren H. S.; Meng, Y. Shirley, ACS Energy Letters, 2023. The dissertation author was the primary investigator and author of this paper.

Chapter 2 A Highly Utilized and Practical Lithium-Sulfur Cathode Enabled in All-Solid-State Batteries

Introduction

In the last decade, the need for safe and cost-effective energy storage systems has grown significantly. By 2030, the global demand for lithium-ion batteries is projected to double from 2.8 to 6 TWh[56], exceeding the projected supply. Due to the increasing adoption of electric vehicles and electrified aviation, much of this demand is driven by the transportation sector. While lithium-ion batteries using insertion-type cathodes have made substantial progress in terms of cost and energy density, these cathodes are reaching capacity and performance limitations. These limitations necessitate the development of alternatives that are safer, lightweight, with lower cost to further advance electrification technologies.[57,58] All-solid-state batteries (ASSBs) using conversion cathodes, such as lithium-sulfur (Li-S), can overcome the shortcomings of current lithium-ion battery technology. Sulfur's high specific capacity (1675 mAh g^{-1})[59] and abundance[60] make it a promising alternative energy storage solution. ASSB architecture also improves operational safety by using non-flammable solid-state electrolytes (SSE) and eliminates the polysulfide dissolution and shuttling effect, arguably the major challenge hindering the commercialization of Li-S in liquid electrolytes[61,62].

With the elimination of polysulfide dissolution in ASSBs, the primary challenge has shifted to addressing the insulating properties and slow kinetics of Li-S cathodes, in addition to their chemo-mechanical degradation from expansion and contraction[63]. The conversion from S_8 to Li_2S, results in an 79% volume change[64] – ten times greater than that of conventional cathodes. This significant volume change generates high internal pressure on the surrounding SSE matrix, leading

to void formation and poor interfacial contact[65]. Consequently, most solid-state studies have adapted cathode fabrication methods from liquid systems. Typically, active materials are incorporated within high surface area carbon hosts through ball-milling[66–69], solution processes[70–72], or vapor deposition[73,74] as a means to increase conductive interfaces and constrain volume changes. Nevertheless, these methods have resulted in inconsistent utilization and cycle life. Given the large amount of carbon typically used, inadequate ionic networks and insufficient contact to sustain conversion are likely responsible. Strategies like heat treatments[75] or creating 3D solid-electrolyte structures[76] demonstrated exciting proof-of-concepts to enhance interfacial contact, but their practicality remains uncertain. Incorporating catalysts has been found to improve conversion kinetics[77,78], although using critical elements like cobalt compromises the low-cost novelty of the Li-S system. While some of these approaches have shown improvement compared to the liquid system, high areal loadings with long cycle life necessary for practicality, have yet to be demonstrated.

Li-S conversion requires "triple-phase" contact between the active materials, ionic and electronic network.[63,79] This is easier to achieve in liquid systems, as liquid electrolyte can flow through electrode pores. In ASSBs, intimate solid-solid contact can be limited and dependent on cathode architecture, including optimal particle sizes and their distribution. Ideally, a uniform distribution of active materials, SSE, and carbon should be achieved. Occasionally, this can promote decomposition or redox activity when using sulfide-based SSEs[71,80,81], formally associated with generating irreversible decomposition products at high voltages[82], especially with high surface area carbon[83]. However, the lower operating voltage of sulfur is more compatible with the lower oxidation stability of sulfide-based electrolytes, where incomplete redox may be

reversible. Therefore, leveraging the redox activity of sulfide SSEs could enhance the reaction kinetics of sulfur and Li_2S. Additionally, facilitating reactions between the cathode materials and sulfide SSEs can result in beneficial interfacial properties[70,84]. To enable a practical high loading Li-S ASSBs, new design strategies are required. Further, to maintain low-cost and make Li-S relevant for industry, the cathode design should be scalable, without relying on additives beyond the active materials, conductive agent, and SSE. This requires a deeper understanding of the potential reactivity between SSEs and Li-S cathodes, and how their coupled redox mechanisms drive electrochemical performance and chemo-mechanical behavior.

In this chapter, we aim to develop a Li-S cathode that addresses the interfacial, kinetic, and (chemo)mechanical challenges when implemented in ASSBs, where cathode and cell level design strategies were implemented to improve utilization and cycle life (**Fig.2.1**). A single step mechanochemical process enabled the formation of ionically conductive interphases by facilitating bonding between the SSE and sulfur particle surface. The sulfur-SSE interphase and uniform carbon network creates a microstructure with many "triple-phase" sites for conversion. To improve cycle life, three features were enabled. First, activation of the sulfide SSE redox activity was accomplished using the single-step synthesis process and was confirmed to be reversible within the sulfur and Li_2S voltage windows. Using X-ray absorption spectroscopy (XAS), we deconvolute these capacity contributions and validate electrochemical reversibility with both sulfur and Li_2S. Second, tailoring cathode particle size to the micron scale created a cathode microstructure with reduced ionic tortuosity, enabling stable high rate cycling. Third, morphological analysis confirms that both sulfur and Li_2S cathodes undergo significant volume change. However, these volume changes were found to alleviate internal pressures, especially when paired with high-capacity

anodes like silicon. As a result, unrivaled room temperature performance was demonstrated, achieving 500 cycles with 85% retention. Further, high loading sulfur cathodes up to 11 mAh cm^{-2} delivered stable cycling for over 140 cycles. A 'proof of concept' Li_2S anode-free pouch cell delivers a high reversible capacity of 900 mAh g^{-1} under practical operating conditions. This work contributes new insight on cathode and cell level design considerations, supporting the development of practical and high energy dense ASSBs using Li-S conversion chemistry.

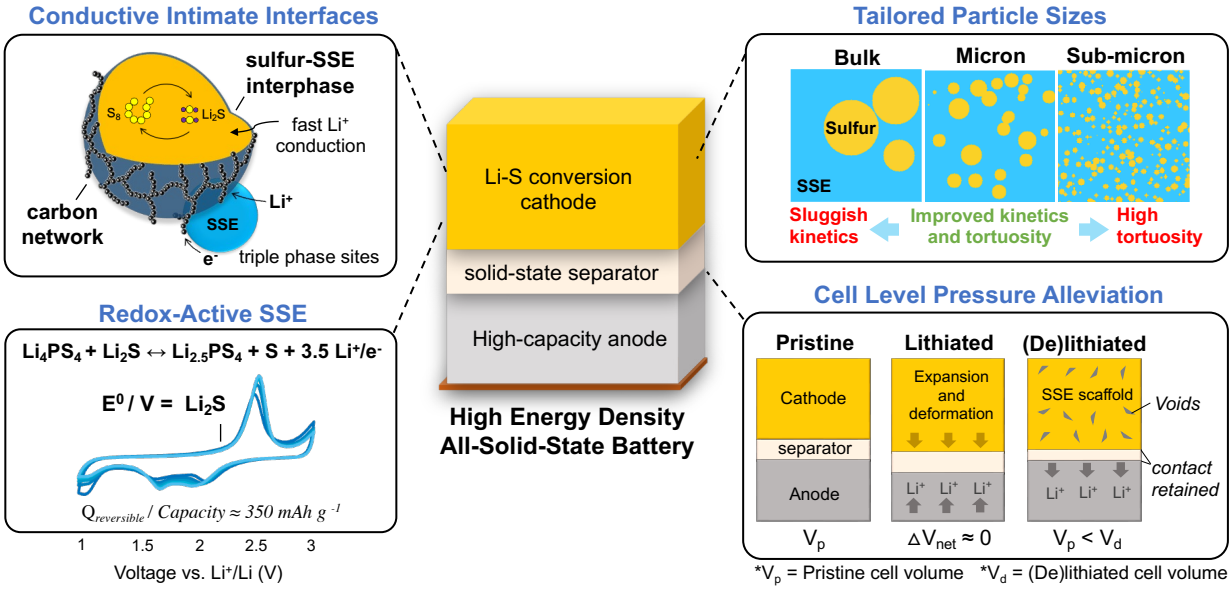

Figure 2.1: Key features required to enable high energy density ASSBs with Li-S conversion cathodes, improving both utilization and cycle life under practical operating conditions.

Results and Discussion

Cathode composite architecture including conductive interfaces are one of the critical components to enable high performing Li-S ASSBs. The potential reactivity between the active materials and the sulfide-SSE were investigated using a one-step mechanochemical milling procedure. To prove the effectiveness of this approach, two common fabrication methods were considered: hand-mixing and a multi-step milling process. Schematics illustrating each method

and their expected distribution are shown in **Supplementary Figure 2.1,** where unmodified elemental sulfur, argyrodite Li_6PS_5Cl (LPSCl), and acetylene black (AB) carbon were used.

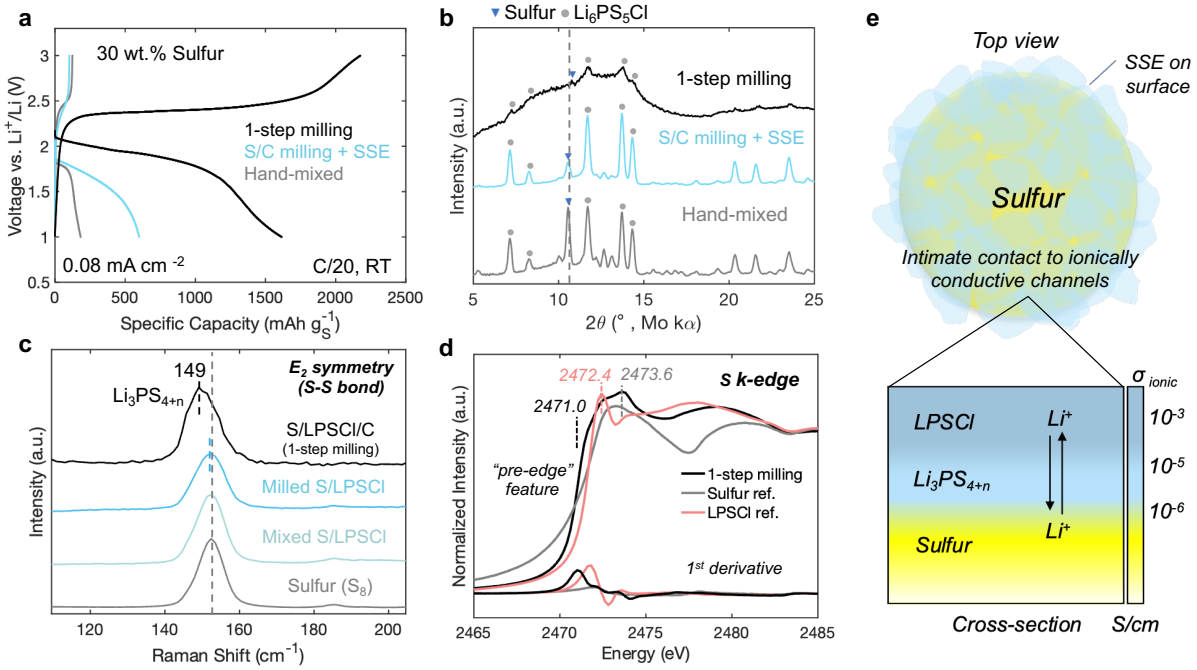

Figure 2.2: Characterizing the sulfur cathode composites after synthesis**.** a) Voltage profiles and (b) X-ray diffraction (XRD) spectra of the cathode preparation methods. c) Raman spectroscopy and (d) X-ray absorption spectroscopy (XAS) of the one-step milled composite. e) Schematic of the surface reaction with LPSCl bonded on the sulfur surface due to the one-step milling procedure.

Increases in sulfur utilization and discharge capacity are attained by introducing high energy milling steps to the fabrication process (**Figure 2.2a)**. This is likely from improved distribution and more contact points for conversion. The multi-step process however suffered from low utilization, implying insufficient sulfur-SSE contact. It was also irreversible, marked by a low conversion efficiency (CE) of 17%. Commonly observed in prior works[68,73,80,85,86], a low CE suggests insufficient mass transport to reconvert Li_2S back to sulfur, usually requiring high activation potentials to do so[87]. The low CE can also be from the isolation of cathode particles and active surface areas after volume expansion. A comparison between hand-mixing and ball-milling has been previously investigated by Ohno *et al.*, where ball-milling achieved higher capacities,

resulting in a CE of 100%.[88] However, the single-step method used here delivered a discharge capacity near the theoretical (1615 mAh g^{-1} at 25°C) and a CE of 128%, meaning this method also activated LPSCl redox activity. A high discharge capacity coupled with SSE redox activity, suggests that this fabrication strategy produced an architecture to facilitate improved ionic/electronic transport and sufficient "triple phase" contact sites for Li-S conversion.

Figure 2.2b shows the diffraction patterns of the prepared composites. With all three methods, LPSCl and sulfur are detectable. Only the one-step method facilitated amorphization of the composite. Since the diffuse scattering of AB carbon can mask diffraction peaks, the milling procedure was done without carbon (i.e., S/LPSCl) (**Supplementary Figure 2.2a**), where the full width at half maximum (FWHM) still increased for both characteristic peaks of sulfur and LPSCl. Amorphization, evidenced by peak broadening, can be explained from the high energy milling process, which can induce disorder.[89] The amorphization of sulfur during the fabrication process is extremely advantageous since crystalline sulfur (cyclo-S_8) requires large activation energies to break the covalent bonds between sulfur atoms[90]. Amorphous composites can lower the energy barrier for conversion and have been attributed to improved electrochemical performance[91,92]. To better understand the composite amorphization, thermogravimetric analysis (TGA) was used to quantify elemental sulfur (**Supplementary Figure 2.3**), which should fully sublime around 350°C[93]. However, 6.5 wt.% of sulfur is unaccounted for after sweeping to 450°C, indicating alteration of the S_8 bonding environments and possible reaction with LPSCl. To investigate this, Raman spectroscopy was conducted focusing on the S-S bonding region centered at 152 cm^{-1}, which is a signature peak of E_2 symmetrical bending[94]. In this region, a redshift is observed with the milled S/LPSCl and one-step milled composites (**Figure 2.2c)**. The addition of carbon further

promotes this reaction. The S-S bending at lower wavelengths reveal the formation of lithium polysulfidophosphates (Li_3PS_{4+n}), where elemental sulfur bonds with the sulfur at the PS_4^{3-} terminals of LPSCl.[70,84] This observation is complimented by the reduction of the symmetric P-S stretching of the thiophosphate unit (PS_4^{3-}) in LPSCl at 425 cm $^{-1}$ (**Supplementary Figure 2.2b)**, suggesting that the number of sulfur atoms bonded at each terminal sulfur atom may vary. The formation of these intermediate compounds (Li_3PS_{4+n}) typically requires solvents to facilitate the reaction[70,84]. Here, we enable this interfacial reaction with a fully scalable single-step dry process. The bonding between the thiophosphate units of LPSCl and sulfur ensures intimate contact of the sulfur/SSE interface and rationalizes the high sulfur utilization shown in **Figure 2.2a**.

The X-ray absorption near-edge structure (XANES) region is useful in examining oxidation states and local bonding environments. Synchrotron radiation at the Sulfur K-edge was measured for the sulfur composite and reference samples (**Figure 2.2d**). Two main peaks can be observed for elemental sulfur at 2473.6 eV and LPSCl at 2472.4 eV. A "pre-edge" feature at 2470.1 eV is also evident from 1st derivatives of the spectra. "Pre-edge" features indicate a reduction of the sulfur oxidation state and have been observed for long chain polysulfides (Li_2S_y)[95]. The "pre-edge" observed here is likely from long chains of sulfur in Li_3PS_{4+n}. Ionic conductivity of the S/LPSCl composites after various milling durations were also measured, where an increase is observed after 1 hour and saturates near 2×10^{-5} S cm $^{-1}$ with continued milling (**Supplementary Figure 2.2c**). The increase in ionic conductivity confirms the formation of an ionically conductive phase using the mechanochemical process. However, particle morphology and chemical composition of this phase is elusive using conventional scanning electron microscopy (SEM). Therefore, low-dose cryo-TEM, high-angle annular dark-field scanning transmission electron

microscopy (HAADF-STEM) imaging, and elemental mapping was conducted on multiple particles (**Supplementary Figure 2.4 and 2.5**). Line scan results reveal the particle is sulfur with LPSCl on the surface (**Supplementary Table *2.1***). These results corroborate the interfacial reaction between sulfur and LPSCl, creating an ionically conductive phase on the sulfur particle surface. The tailored interface lowers the energy barrier for lithiation, facilitating fast lithium transport from the SSE matrix into the sulfur bulk as illustrated in **Figure 2.2e**.

The interaction between LPSCl and Li_2S was also investigated. A comparison between cathode preparation methods was conducted, where comparable trends seen with sulfur is observed with Li_2S (**Supplementary Figure 2.6**). Hand-mixing the composite fails to cycle, and the multi-step process delivers low utilization coupled with large polarization. The one-step method, however, delivers a high specific capacity of 723 mAh g^{-1} with a high coulombic efficiency of 99.3%, indicating good reversibility. With the Li_2S cathode, the synthesis method resulted in the decomposition and amorphization of LPSCl, evidenced by undetectable peaks in the diffraction pattern and a shift of P-S stretching in PS_4^{3-} from 425 cm^{-1} to 418 cm^{-1}, assigned to Li_3PS_4 (LPS)[96] (**Supplementary Figure 2.7**). These results suggest that Li_2S reduced LPSCl to LPS. Despite this decomposition, the Li_2S cell exhibits stable cycling, where additional plateaus present in the voltage profile after the 1st cycle (**Supplementary Figure 2.8**) indicating that this approach also activated redox activity from the SSE decomposition products and is electrochemically reversible.

Evaluating LPSCl redox activity and electrochemical reversibility. The redox activity of sulfide SSEs has been responsible for delivering capacity beyond the theoretical when paired with Li-S cathodes[70,71,74] and associated with irreversible electrochemical behavior[97]. Often overlooked

in literature, deconvoluting the capacity contribution between sulfur and SSE is essential in accurately quantifying utilization and effectiveness of the cathode architecture. To isolate this capacity contribution and study its potential reversibility, cells with just LPSCl and carbon were evaluated.

LPSCl, like many sulfides, exhibit a narrow stability window, reducing at 1.3 V and oxidizing at 2.3 V vs. Li/Li^+ [81,83]. This is reinforced by constant current discharge and charge results, where the reduction and oxidation capacity of 115 mAh g^{-1} and 355 mAh g^{-1} was obtained (**Figure 2.3a**). These capacities obtained from LPSCl redox, explain the additional charge capacity observed in the sulfur cells, which is also recoverable upon subsequent discharge. Reversible behavior of LPSCl is also observed within the Li_2S voltage window, delivering a high reversible capacity of 400 mAh g^{-1} (**Figure 2.3b**). Assuming this behavior is consistent when paired with Li-S cathodes, expected redox products of the LPSCl electrolyte can be predicted. Complete oxidation of LPSCl forms sulfur, LiCl, and P_2S_5 with reduction products being Li_2S, LiCl, and Li_3P.[81,97] In both redox pathways, LPS is formed intermediately. From the experimentally obtained capacities, the expected reaction can be hypothesized where upon discharge and charge, a lithium rich Li_4PS_4 and lithium deficient $Li_{2.5}PS_4$ can be formed.

$$Li_6PS_5Cl + 1\ Li^+/e^- \longrightarrow Li_2S + Li_4PS_4 + LiCl$$
$$Q_{red} / \textit{ Capacity} \approx \textit{100 mAh } g^{-1}$$

$$Li_2S + Li_4PS_4 + LiCl \longrightarrow Li_{2.5}PS_4 + S + 3.5\ Li^+/e^- + LiCl$$
$$Q_{ox} / \textit{ Capacity} \approx \textit{350 mAh } g^{-1}$$

$$Li_2S + Li_4PS_4 \leftrightarrow Li_{2.5}PS_4 + S + 3.5\ Li^+/e^-$$
$$Q_{reversible} / \textit{ Capacity} \approx \textit{350 mAh } g^{-1}$$

The electrochemical cycling results of LPSCl allow us to isolate sulfur utilization. In this system, stable sulfur utilization above 80% is achieved (**Figure 2.3c**). This can be attributed to the enhanced ionic transport and ionically conductive interfaces formed during synthesis. Additionally, between this cutoff voltage, cyclic voltammetry sweeps of both sulfur and LPSCl composites reveal their coupled reversible behavior (**Figure 2.3d**). The upper voltage cutoff below 3.5 V limits the complete oxidation of LPSCl, preserving ionic conductivity with continued cycles. The high oxidative tendency of LPSCl at 2.3 V vs. Li/Li^+ can be effective at reducing the activation potential of Li_2S. This was already observed with the Li_2S cathode, where the activation voltage observed in this work is 2.4 V, without requiring the use of catalysts or kinetic promoters.

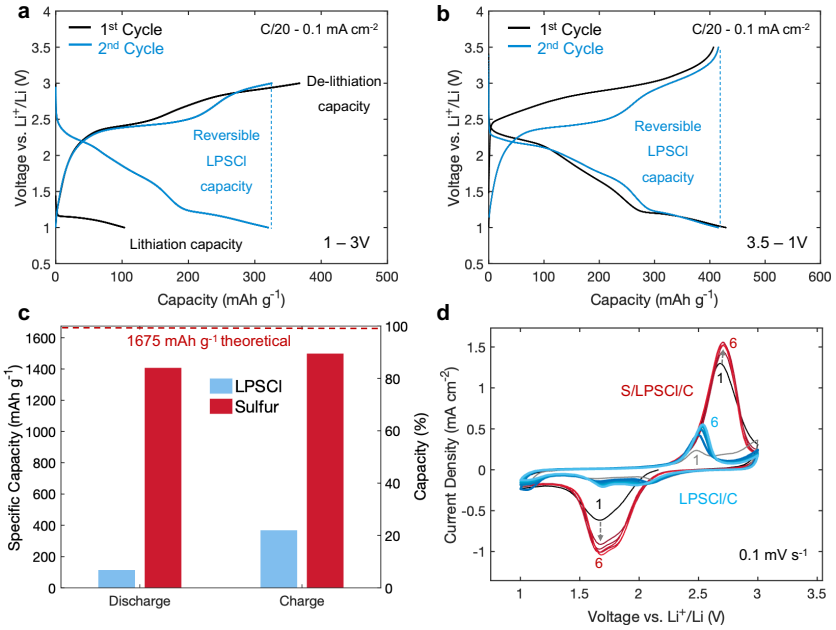

Figure 2.3: Evaluating LPSCl redox activity. Voltage profiles of LPSCl/C composites evaluated under (a) sulfur and (b) Li_2S voltage limits. c) Specific capacity, and capacity contributions of sulfur and LPSCl. d) Cyclic voltammetry of S/LPSCl/C and LPSCl/C composites.

To verify the reversibility of the cathode composites, redox products during the 1st formation cycle were investigated. *In-situ* electrochemical impedance spectroscopy (EIS) was performed on the sulfur cathode at each state of charge (**Figure 2.4a**). After discharge, impedance

growth attributed to the charge transfer resistance from Li_2S formation was observed. After charging, the charge transfer resistance reduces and returns near the pristine state, indicating good reversibility. Post-mortem analysis was conducted to confirm Li_2S formation and conversion, where diffraction peaks attributed to nanocrystalline Li_2S are detected in the XRD spectra after discharge (**Figure 2.4b)**, supporting the high utilization of sulfur. After charging, Li_2S is undetectable, indicating its complete oxidation, while the formation of sulfur at 10.5° 2θ is observed. Given the high charge capacity, the low peak intensity and amorphous background suggest that the reformed sulfur is amorphous as in the pristine state. This also suggests the sulfur-SSE conductive interphase is preserved with cycling. TGA results at the discharged and charged states further reinforce high sulfur utilization and the reversibility of this system (**Figure 2.4c**).

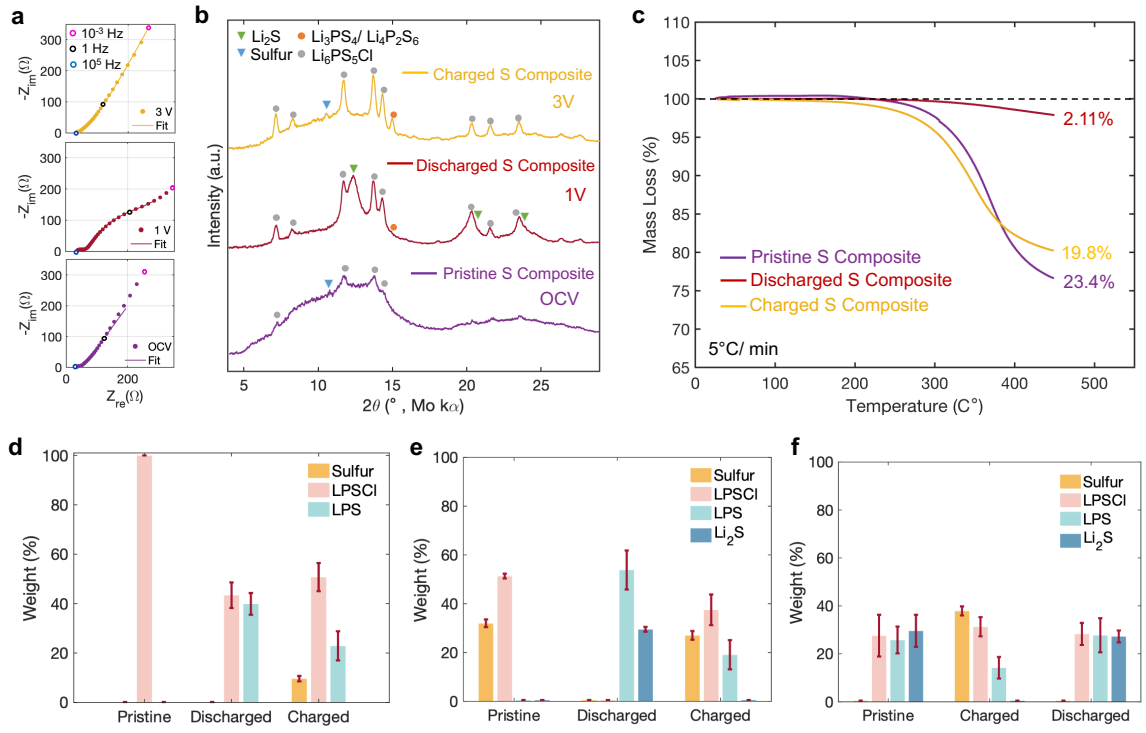

Figure 2.4: Evaluating LPSCl redox activity. Voltage profiles of LPSCl/C composites evaluated under (a) sulfur and (b) Li_2S voltage limits. c) Specific capacity, and capacity contributions of sulfur and LPSCl. d) Cyclic voltammetry of S/LPSCl/C and LPSCl/C composites.

However, fully deconvoluting the redox products between LPSCl, sulfur, and Li_2S are challenging. Therefore, XANES spectra at the Sulfur K-edge were measured for all the composites with reference spectra reported in **Supplementary Figure 2.9**. Using the reference spectra, linear combination fit (LCF) analysis can be used to quantify species.[98,99] These fitting spectra are reported in **Supplementary Figure 2.10**, **2.11,** and **2.12**. As hypothesized from the electrochemical results for the LPSCl/C case, 39.9 wt.% of LPS is predicted after discharge, suggesting that half of the LPSCl formed the lithium rich $L_{4.1}PS_4$ phase. After charging, 9.7 wt.% is sulfur with some LPS reforming LPSCl (**Figure 2.4d**). These results support the formation of LPS as a redox intermediate, where its reversible redox behavior likely improves the kinetics of Li_2S oxidation. LCF results for the sulfur and Li_2S system also support the reversible electrochemical behavior. For the XANES sulfur fitting results in **Figure 2.4e**, 29 wt.% of Li_2S is estimated after the initial discharge, indicating good conversion efficiency. After charging, Li_2S was converted back to sulfur. The additional capacity observed in the formation cycle can be attributed to LPS and a small amount of sulfur from LPSCl oxidation. These results coupled with EIS, XRD, and TGA support the high conversion efficiency attributed to the formation of the ionically conductive interphase layer and the redox activity of the LPSCl electrolyte. Similar conclusions can be drawn for the Li_2S system**.** Complimenting findings revealed by XRD and Raman, half of the LPSCl decomposes to LPS after synthesis (**Figure 2.4f**). Nevertheless, the amorphous LPS/LPSCl mixture retains its ionic conductivity, supported by the Li_2S electrochemical performance and XANES results. A complete summary of the fitting results can be found in Supplementary Table *2.2*.

The previous electrochemical performances were obtained using unmodified bulk sulfur and Li_2S, where particle sizes were on the order of 100 microns for sulfur (**Supplementary Figure**

2.13a) and 30 microns for Li_2S (**Supplementary Figure 2.14**). These sizes, while sufficient for low cycling rates, need to be reduced to improve Li^+ transport and enable higher rate operation. Sulfur particle sizes were produced on the micron and sub-micron scale (**Supplementary Figure 2.13**). Given the many possible compositions, geometrical modeling was conducted to aid in experimental design, connecting particle size and composition to active surface areas and transport properties. Sulfur cathode geometries were stochastically generated, with the sulfur as spherical particles and the carbon additives as aggregates (**Figure 2.5a**). To compare with experimental capabilities, particle size ranges for bulk, micron, and sub-micron sulfur was 25 to 50 μm, 0.5 to 5 μm, and 0.25 to 0.5 μm, respectively. **Figure 2.5b** shows the evolution of the active surface area as a function of AM content. The reported values are the average over three repetitions. Intuitively, the sub-micron electrode exhibited the highest active surface area for all AM contents (%), followed by the micron sulfur, and bulk sulfur electrode. Therefore, sub-micron sulfur particles are expected to achieve the highest utilization due to more SSE contact. The tortuosity of the LPSCl phase was explored with the reported value being the average tortuosity in all directions. Surprisingly, the micron sulfur electrode exhibits the lowest ionic transport tortuosity, with all cases obtaining similar results until higher AM contents (**Figure 2.5c**). The geometrical modeling results suggest that sub-micron particles may be the best choice to achieve high utilization, yet high active wt.% may be challenging to implement since the ionic transport tortuosity increases drastically after 50 wt.%. Despite the expected high utilization with sub-micron particles from higher surface areas, it must be noted that the geometrical modeling does not consider the (chemo)mechanical effects from lithiation.

To validate the modeling results, room temperature electrochemical performance was conducted for each particle class in LiIn half cells. All particle sizes deliver comparable discharge capacities during the 1st formation cycle at low rates (0.08 mA cm $^{-2}$) (**Figure 2.5d**). The sub-micron sulfur cell delivers the highest discharge capacity of 1694 mAh g^{-1}, beyond the theoretical. This was followed by micron and bulk sulfur which delivered 1615 mAh g^{-1} and 1500 mAh g^{-1}, respectively. This suggests that more LPSCl redox activity can be activated with higher surface area particles. Higher charge capacities are also observed for all cells, reinforcing the additional capacity from the LPSCl electrolyte. The additional charge capacity results in a higher discharge capacity from the 2nd formation cycle with a reduction in cell polarization from 577 mV to 452 mV (**Supplementary Figure 2.15a**). The reduced cell polarization could either be from LPSCl redox products or from potentially beneficial (chemo)mechanical behavior. Rate capability was also conducted up to 1C (1.6 mA cm $^{-2}$) (**Supplementary Figure 2.15b)**. The current density at 1C is beyond the critical current for the LiIn anode (~ 1 mA cm $^{-2}$)[100], however, all three cells deliver reasonable utilization at all rates, with bulk sulfur delivering the lowest due to kinetic limitations. Since LPSCl was found to contribute capacity, the specific capacity considering both sulfur and LPSCl masses show reasonable utilization (700 mAh g^{-1}) for both micron and sub-micron at these rates. This is critical for solid-state, as the catholyte is usually considered inactive, responsible for "dead weight" within the cell. In this work, the catholyte contributes electrochemically to the overall cell capacity.

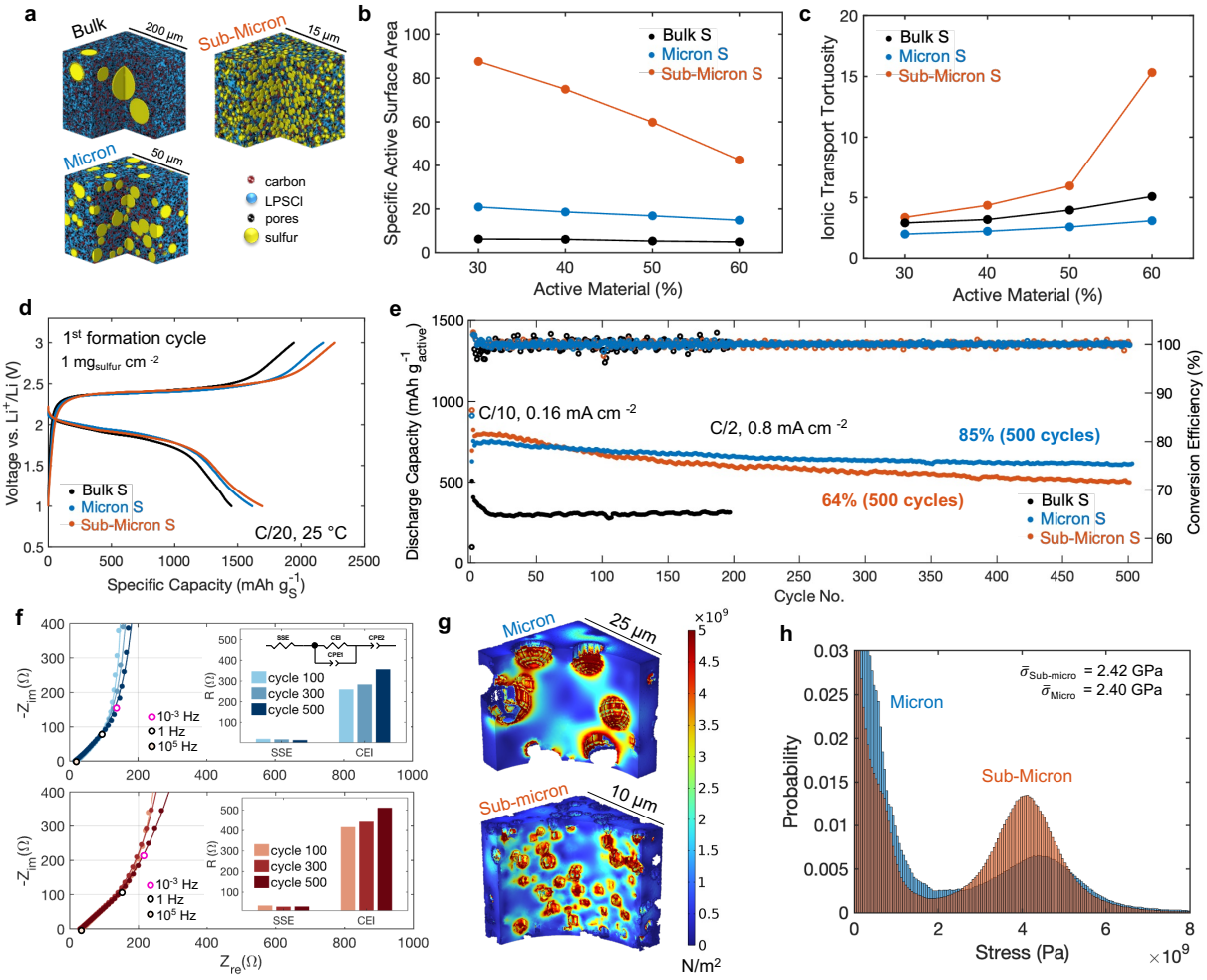

Figure 2.5: a) Geometrically modeled sulfur composite electrodes. b) Specific active surface area and (c) ionic transport tortuosity as a function of AM content (%) and particle size. d) First formation cycle voltage profiles. e**)** Long-term cycling stability at C/2. f) Nyquist plots. g) Distribution of the von Mises stress. h) Predicted variation of maximum von Mises stress.

Longer term higher rate cycling was evaluated to investigate the particle size effect on cycle life (**Figure 2.5e**). The bulk sulfur composite exhibits fast decay, due to longer Li^+ transport lengths from large sulfur particles and poor contact observed after densification (**Supplementary Figure 2.13g)**. Despite achieving the highest utilization, the sub-micron sulfur composite delivers 64% retention, with micron being the most stable system, achieving 85% retention after 500 cycles. The retention of the sub-micron cells is significant for Li-S in ASSB at room temperature. Nevertheless, a 20% increase in retention with micron scale particles is a large improvement. The

capacity fade of sub-micron cells may be due to excessive decomposition from higher surface area between the carbon and SSE. To test this, cells were constructed with the micron sulfur composite using carbons that possess different specific surface areas and morphologies (**Supplementary Figure 2.16**), each chosen to intentionally facilitate more SSE redox activity. Increasing the carbon surface area increased utilization, mainly from the SSE, but showed no impact on cycling stability. This means the decay observed with the sub-micron sulfur composite is likely of (chemo)mechanical origin, causing degradation at sulfur/SSE particle interfaces. This interfacial degradation should result in impedance growth, where EIS was measured after 100, 300, and 500 cycles (**Figure 2.5f**). The intermediate frequency range was assigned to the cathode electrolyte interphase (CEI).[101] The sub-micron sulfur cells do possess higher resistance after 100 cycles, attributed to more mechanical degradation with continued cycling. However, these results differ slightly. Cross-section scanning electron microscopy (SEM) imaging may be useful, although both composites were found to show indistinguishable morphology (**Supplementary Figure 2.17**). Therefore, mechanical-based simulations using the generated electrodes in **Figure 2.5a** may shed insight on the accumulated stresses at these interfaces.

Sulfur cathodes undergo large volume expansion upon lithiation[102] resulting in internal stresses at their interfaces. To simulate this mechanism, volume changes were estimated based on % utilization for each particle size using 1st cycle discharge capacities based on sulfur mass and subtracting the expected capacity from LPSCl (**Supplementary Figure 2.18**). Simulations were conducted using finite element method (FEM) where the sulfur particles underwent the prescribed volume expansion derived from the electrochemical results. Parameters and equations used in the simulations can be found in Supplementary Table *2.3* and *2.4*. **Figure 2.5g** displays the distribution

of maximum von Mises stress on the SSE matrix, where for both micron and sub-micron cases, stresses beyond 5 GPa were predicted. A bimodal stress distribution shown in **Figure 2.5h**, highlights most of the SSE matrix does not experience stress since only 30 wt.% of sulfur is used in the simulation. However, at the cathode interface, the sub-micron sulfur composite experiences a higher frequency of stress from more volume expansion and increased tortuosity. Stress accumulated at the boundaries of the sulfur particles can propagate when these particles are in proximity, creating thinner SSE channels that experience much higher stress versus the bulk. If SSE fracture occurs, pore formation is possible after (de)lithiation. These simulations only capture stress after the 1st lithiation. However, SSE degradation is expected to accumulate with cycling, disrupting ion conduction pathways and leading to more capacity fade as observed in **Figure 2.5e**. Electrochemical evaluation, coupled with FEM simulations uncover that sub-micron sulfur particles create a microstructure with high electrode tortuosity, resulting in higher interfacial stresses and faster capacity decay. Previous studies have required nano-scale particles to achieve reasonable utilization[103–105]. However, in this work, micron-scale particles can deliver both high active surface area and low electrode tortuosity, balancing both high utilization and stable cycling, critical for practical Li-S cathodes.

In ASSBs, Li-S cathodes are expected to experience (chemo)mechanical degradation from their large volume changes. This will result in stresses on various interfaces as simulated above. Electrochemical performances of sulfur, Li_2S, and LPSCl were found to be highly reversible, but this impact on cathode morphology remains unknown. To visualize this, cross-sectional SEM images were prepared for both micron sulfur and Li_2S cells at each state of charge. Both pristine sulfur and Li_2S cathodes exhibit a dense composite structure, possessing a thickness of 26 μm and

45 μm, respectively, and good interfacial contact (**Figure 2.6a and 2.6b**). Calculations were done to estimate the volume change (%) as a function of sulfur cathode wt.% assuming complete lithiation (**Supplementary Figure 2.19**). Here, 25.8 vol.% change is expected, resulting in a thickness increase to 32.7 μm, close to the observed result. The lithiation capacity of this cell was 1.22 mAh. Therefore, the thickness increase of the cathode equates to 4.9 μm mAh^{-1}, which is the expected thickness growth of Li metal with cycling[106]. This suggests that lithiating the sulfur cathode can compensate the volume reduction of stripping Li metal. After completing the 1st cycle, the sulfur cathode thickness was retained but can be resolved by an increase in porosity. These results reveal that during lithiation, the resulting stress on the SSE matrix causes it to plastically deform to accommodate particle expansion. The deformed structure preserves intimate contact to the separator layer and assists structurally during cycling. These findings can also explain the reduction in polarization after the 1st cycle, where subsequent volume expansion is likely supported by the pre-deformed SSE structure. The plastic deformation of the SSE matrix is not surprising, as the simulated stresses estimated above is near the shear modulus of LPSCl[107].

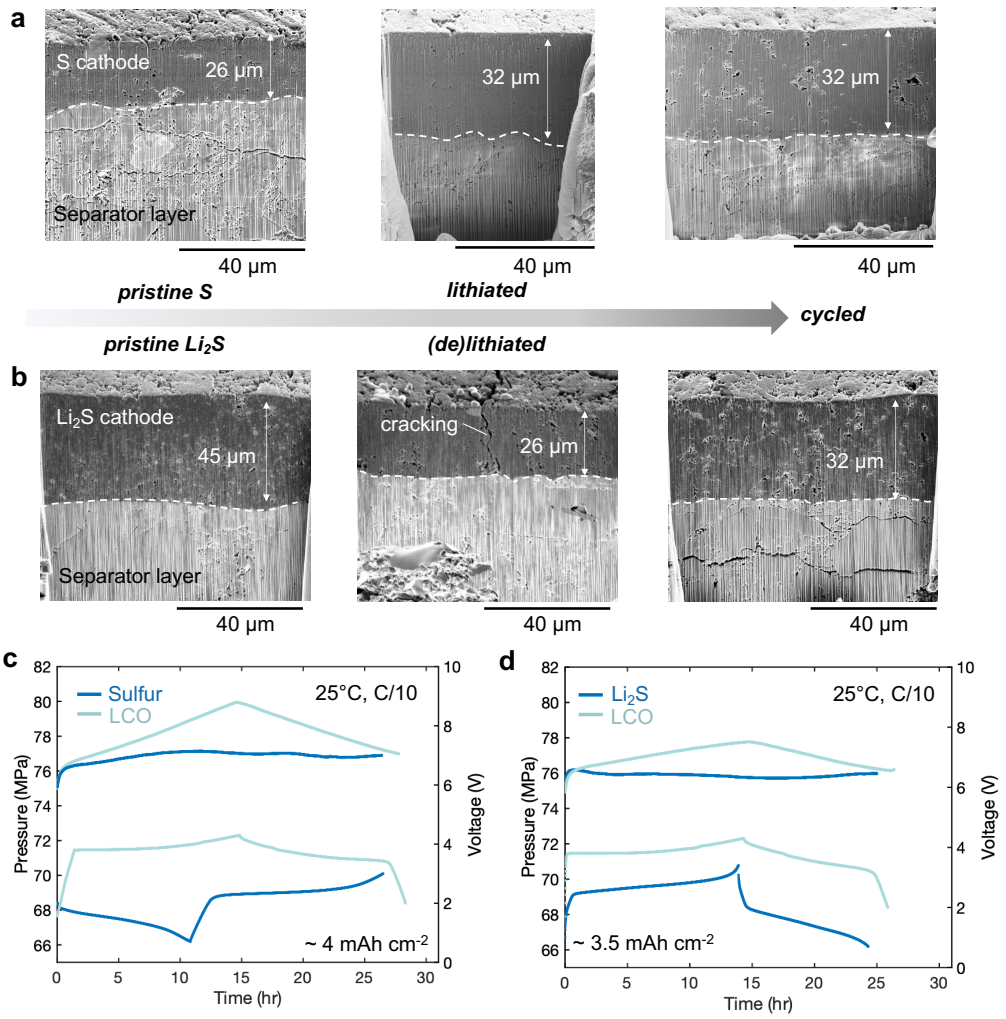

Figure 2.6: Quantifying cathode and cell level volume changes. Cryo-FIB images of the (a) micron sulfur and (b) Li_2S cathode composite at various states of charge. c) *Operando* pressure monitoring of LCO and Sulfur using a lithiated silicon anode and of (d) LCO and Li_2S using a µSi anode during the first formation cycle.

The Li_2S cathode is expected to shrink after (de)lithiation. Shown in **Figure 2.6b**, the Li_2S cathode thickness decreases drastically (~ 40%), where columnar cracking is observed in the cross-section as well as on the surface (**Supplementary Figure 2.20**). This cracking is likely strain induced from lithium removal. This morphological phenomenon has been observed in ASSBs using silicon anodes [108] and these results suggest that this (chemo)mechanical behavior is ubiquitous in composite conversion electrodes when constrained to 2D interfaces. After completing one cycle, the cathode morphology is however, reversible, returning close to the

pristine state and is a similar thickness as the electrochemically formed Li_2S in **Figure 2.6a**. These results provide two key insights. First, conversion cathodes can alleviate anode volume changes. Second, Li_2S cathodes inherently face more mechanical challenges compared to sulfur due to strain induced cracking after (de)lithiation.

To demonstrate the pressure alleviation proof of concept, *operando* pressure monitoring was conducted comparing $LiCoO_2$ (LCO), sulfur, and Li_2S when paired with μSi and lithiated Si anodes. LCO will expand due to Jahn-Teller distortions[109], although volume expansion is 10 times less than Li-S cathodes. Si is expected to undergo large volume expansion upon lithiation but will be lower than expected due to the constrained 2D interface[108]. Nevertheless, pressure imbalance and resulting (chemo)mechanical degradation is one of the most challenging aspects for solid-state silicon anodes.[110] In theory, using conversion cathodes can relieve internal stresses caused by cycling and to achieve high energy density, high capacity cathodes should be paired with high capacity anodes. Since a lithium source is required for sulfur, cells were assembled using the lithiated silicon anode, where minimal pressure changes with sulfur were observed (**Figure 2.6c**). However, the LCO cell pressure increases five times that observed for the sulfur case, with pressure fluctuations consistent with previous studies[111]. When using the μSi anode with Li_2S, almost zero pressure variation is detected during the 1st formation cycle (**Figure 2.6d**). The LCO cathode, however, increases by 3 MPa during the charge. Pressure changes from high-capacity anodes can be successfully compensated using conversion cathodes that are highly utilized. This improves cycle life and mitigates cell 'breathing' during cycling, an important consideration for higher loading cells and when integrating cells into pack level architecture.

High loading cathodes are necessary to achieve high energy density. Therefore, cells with increasing sulfur loadings were constructed and first paired with the LiIn alloy (**Figure 2.7a**). Areal capacities up to 11 mAh cm $^{-2}$ with a discharge capacity of 1314 mAh g^{-1} was obtained (**Figure 2.7b**), although with a slight increase in polarization, attributed to the high sulfur loading of 7 mg cm $^{-2}$ evaluated at room temperature. Due to the limited critical current density of LiIn alloys, cycling performance of this high loading system was evaluated at 0.52 mA cm $^{-2}$ (**Figure 2.7c**), showing minimal decay, with 86.8% retention after 140 cycles. The ability to achieve stable cycling at 11 mAh cm $^{-2}$ at room temperature, demonstrates the effectiveness of the cathode microstructure. To overcome the low current density of LiIn, free standing cathode films were fabricated via dry process method and paired with a Li_2Si anode (**Figure 2.7d**). These cells were found to deliver reasonable capacities up to 1C (5.5 mA cm $^{-2}$) as shown in **Figure 2.7e**, with full recovery at C/20 (0.3 mA cm $^{-2}$). This dry process sulfur Li_2Si system also demonstrates stable cycling performance at 7.4 mAh cm $^{-2}$, resulting in 77.4% retention after 150 cycles at 1.5 mAh cm^{-2} current densities (**Figure 2.7f**).

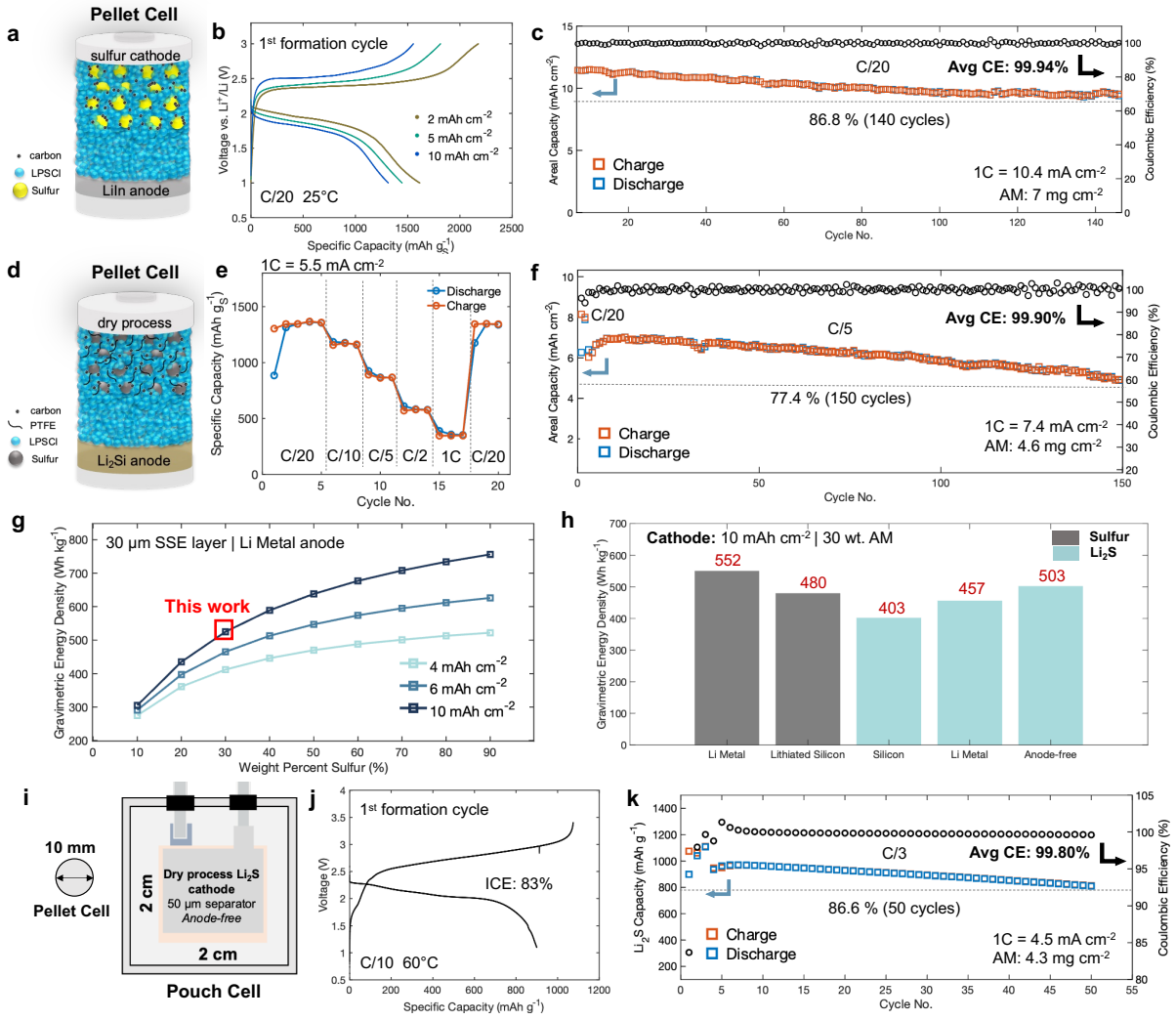

Figure 2.7: Sulfur and Li_2S electrochemical performance with energy density outlook.

Pouch cell form factors utilizing thick dry process cathodes, thin separator layers, and high-capacity anodes are necessary to achieve high gravimetric energy densities in all-solid-state.[112] In addition, high areal capacity and active weight percentages are also required. Illustrated in **Figure 2.7g**, even lower weight percentages of sulfur at 10 mAh cm $^{-2}$ can realize 500 Wh kg $^{-1}$ and is likely a more promising approach than increasing the weight percentage of sulfur. This is because after lithiation, the volume of SSE compared to lithiated sulfur will reduce. Despite sulfur possessing a higher specific capacity than its Li_2S counterpart, anode selection is limited to those

with a lithium source, making lithium metal or pre-lithiated silicon the only practical option, regardless of their high costs and manufacturing challenges. Using the cathode composition reported in this work, Li_2S can achieve over 400 Wh kg^{-1} using silicon as the anode and go beyond 500 Wh kg^{-1} if combined with an anode-free architecture (**Figure 2.7h**). Therefore, a 15 mAh pouch cell was constructed without an anode, utilizing dry process methods, and reducing the separator layer thickness from 500 μm to 50 μm (**Figure 2.7i)**. Industry standard formation rates and cycling protocols were used, where this configuration delivers high utilization (1077 mAh g^{-1}) and ICE of 83% (**Figure 2.7j)**. Stable cycling at C/3 (1.5 mA cm^{-2}) was also achieved at relatively low stack pressures compared to the pellet-type cells (**Figure 2.7k)**.

The electrochemical performances above showcase the versatility of the cathode design methodology, where appropriate synthesis, SSE selection, and optimal cathode microstructure are critical for Li-S chemistry to achieve high utilization and stable cycling. Overall, this approach solves the interfacial, kinetic, and (chemo)mechanical challenges associated with Li-S cathodes in ASSBs. Our work provides a thorough electrochemical, mechanical, and morphological analysis of the critical features required to enable high loading and practical Li-S cathodes. The successful implementation with Li_2Si, μSi, and anode-free architectures presents a promising pathway towards advancing the development of safe and low-cost next-generation high energy density batteries.

Supplementary Information

Materials preparation and composite fabrication. Materials were dried under vacuum at 80ºC if not anhydrous and stored and prepared in an argon-filled glovebox. The solid-state electrolyte separator layer and catholyte used is LPSCl for its high conductivity (3 mS cm^{-1} at room temperature) purchased from NEI Corporation. When used as a catholyte, LPSCl was milled at

400 rpm for 2 hours to reduce its particle size to near 10 microns using a high energy planetary ball mill. For the sulfur cathode, elemental sulfur (99.98%, Sigma Aldrich) was either used as received or milled at 400 rpm for 10 and 24 hours for micron and sub-micron particles. For the Li_2S cathode, Li_2S was either used as received (99.98%, Sigma Aldrich) or milled following similar procedures as sulfur. For electrochemical evaluation, optimal cathode composites were milled for 1 hour (unless otherwise specified) at 500 rpm using a planetary ball mill. Other composite trials were either first milled with carbon and sulfur at 500 rpm for 1 hour, followed by hand mixing the SSE or hand mixing all components for 1 hour. The composites consisted of 30 wt.% cathode active material, 50 wt.% LPSCl and 20 wt.% of a conductive agent (acetylene black, vapor grown carbon fiber, or Ketjen black (EC-600JD)).

Dry process cathode fabrication. Cathode composite powders were mixed with 1 wt.% PTFE (Chemours) in a hot mortar and pestle until dough like consistency is formed. The cathode composite was then hot rolled (MTI corp.) under 60°C conditions with decreasing thickness until a 300 to 200-micron film was made.

SSE film and anode-free layer fabrication. For the SSE film preparation, LPSCl (98 wt.%) and an acrylate binder (2 wt.%) were mixed in p-xylene (Sigma Aldrich). The resulting mixture was casted on a polyethylene terephthalate film and dried under vacuum at 40°C overnight. The slurry for anode-free layer was prepared by mixing carbon black (Imerys), silver nanoparticles, and polyvinylidene fluoride (Solvay) in N-methylpyrrolidone (Sigma Aldrich) at a weight ratio of 69.75:23.25:7.0 as described by Lee et al.[113] This slurry was coated onto a 10 μm thick stainless-steel foil using a doctor blade and subsequently dried in a vacuum oven at 100°C overnight.

Electrochemical Measurements. Electrochemical measurements were performed in custom 10 mm diameter pellet cells constructed out of Grade 5 titanium plungers and polyether ether ketone (PEEK) dies. For cell evaluation and CV measurements, the cathode and separator layers are pressed to 3 tons (375 MPa), while the Li_1In or Li metal anode is pressed to 1 ton (125 MPa) or 0.2 ton (25 MPa), respectively. After assembly, the pellet cells are inserted into custom cell holders and hand tightened to 75 MPa unless otherwise stated. EIS, CV, and LSV measurements were collected using a Biologic SP-300 potentiostat. For EIS measurements, an applied voltage amplitude of 30mV and frequency range of 7 MHz to 20 mHz was used. For LSV and CV measurements, a sweeping rate of 0.1 mV/s was used with voltage ranges between the operating voltage of sulfur (1-3V vs. Li/Li^+). For all electrochemical performance evaluation, elemental sulfur cells were cycled under 75 MPa (unless otherwise stated) at room temperature with either Li_1In_1 or Li_2Si acting as the counter electrode. The method to prepare the Li_2Si anode followed protocols outlined in prior work[114]. Li_2S cells were cycled at room temperature with casted Si anodes as described in previous work[108]. Capacity utilization and cell cycling was evaluated using Neware Instrument cyclers (CT-4008T).

Pouch cell fabrication. Al foil, dry processed Li_2S cathode, SSE film and anode, were stacked, and packed into a pouch. The pouch was vacuum-sealed and pressed to 500 MPa at 80°C using warm isostatic pressure (WIP).

Scanning electron microscopy. Scanning electron microscopy (SEM) was performed on a FEI Apreo and/or FEI Scios DualBeam focused ion beam (FIB)/SEM with 5 kV accelerating voltage

and 0.1 nA beam current for powders and pellets. Powder and pellet samples were prepared in an argon-filled glovebox and transferred using the air-tight transfer arm to avoid any air exposure. For FIB cross-sectional images, milling was done under cryogenic conditions (-180°C) where Ga was used as an ion beam source. Parameters used for all milling conditions of 30 kV, 65 nA, with the subsequent cross-section cleaning performed with 30 kV, 15 to 7 nA, if necessary.

X-ray Diffraction. XRD measurements were collected over a 5 – 50° 2θ range on a Bruker ApexII-Ultra CCD microfocus Rotating Anode instrument with Mo K_α (λ = 0.7107 Å) radiation at the UCSD X-Ray Crystallography Department. Samples were prepared in an argon-filled glovebox using 0.7 mm boron capillaries, and flame sealed to ensure air-tight measurements of sensitive samples.

Transmission electron microscopy. The sample was mounted to an airtight cooling holder from Melbuild to eliminate any contaminations to the sulfur/LPSCl/C samples and transferred to the TEM column directly without any air or moisture exposure. The sample was cooled down to cryogenic conditions (~180°C) and stabilized for additional 30 minutes before electron beam exposure. (S)TEM results were obtained on ThermoFisher Talos X200 equipped with a Ceta camera operated at 200 kV with low dose capability. The energy dispersive X-ray spectroscopy (EDS) characterization is installed with compositional mapping using 4 in-column SDD Super-X windowless detectors. The data acquisition was operated at low dose condition to minimize any beam damage to the sample.

X-ray Absorption Spectroscopy. Tender X-ray absorption spectroscopy (XAS) measurements were conducted at Taiwan Light Source (TLS) beamline 16A1 of the National Synchrotron Radiation Research Center (NSRRC) in Hsinchu, Taiwan. The beamline uses a double-crystal Si (111) monochromator for the photon energy range from 2 to 8 keV. All samples were sealed in a pouch made of 2.5 um thick Mylar® film inside an Ar-filled glovebox to prevent the samples from exposure to air. Each sample was mounted onto the holder and placed in the measuring chamber at an angle of 45° to the incident X-ray beam. The chamber is constantly purged with He to reduce the X-ray attenuation for at least 45 minutes before collecting the XAS data. The Sulfur *K*-edge X-ray absorption near-edge structure (XANES) spectra were collected in the total fluorescence yield (TFY) mode using a Lytle detector with a scanning step of 0.2 eV. The photon energy was calibrated to 2472 eV (maximum in the 1st derivative) at the S *K*-edge using elemental sulfur. The XANES spectra background subtraction, normalization, and the Linear Combination Fit (LCF) were performed on Athena software. [115]

Modeling of sulfur electrode geometries. The electrodes structures were stochastically generated using the MATLAB codes from Duquesnoy et al.[116], with the S as spherical particles, and the carbon additives as aggregates. A volume fraction of 10% was dedicated to pores, the S amount ranged from 30 to 60%, and the volume ratio between the LPSCl and carbon additives was kept constant at 5:2. Three different cases were investigated, Bulk, Micro and Nano, with S radii ranging respectively from 25 to 50 µm, 0.5 to 5 µm, and 0.25 to 0.5 µm. To have a representative volume for each condition, the length of the cubic electrodes was 200 µm for the Bulk, 50 µm for the Micro, and 15 µm for the Nano. For each set of S size and amount, 3 electrodes were generated to obtain statistically relevant observables. The evolution of the active surface area

was monitored as the specific surface area, i.e. the ratio between the number of pixels of S in contact with LPSCl and the total number of S pixels. The tortuosity of the LPSCl phase was investigated using TauFactor[117] in MATLAB, and the reported value is the average value of the tortuosity of the electrolyte phase in all directions.

Finite Elements Method (FEM) Simulations. The electrodes were meshed using the open-access toolbox Iso2Mesh[118] and later imported into COMSOL Multiphysics 6.1. There, using the Solids Mechanics module, the set of parameters and equations in Supplementary Table 2.3 and Supplementary Table 2.4 were set. In the model, the electrode was assumed to be fully compact (no porosity) and the S particles were uniformly lithiated throughout the simulation, leading to a volume expansion made possible with the "Hygroscopic Swelling" node which normally accounts for the volume expansion of solids due to the amount of water. During the simulation, the external boundaries of the electrode were fixed. To determine the analog hygroscopic coefficient of each type of S particles, a 2-D simulation consisting of the exact same model for a single S particle was performed. The hygroscopic coefficient was deemed adequate when the S particle would reach the desired volumetric expansion (controlled here by its radius) at full lithiation. The cases of sub-micro and micron S were investigated through FEM simulations for an AM content of 30 wt.% where three electrodes were used for each case, and the value reported in the manuscript are averaged over all three electrodes.

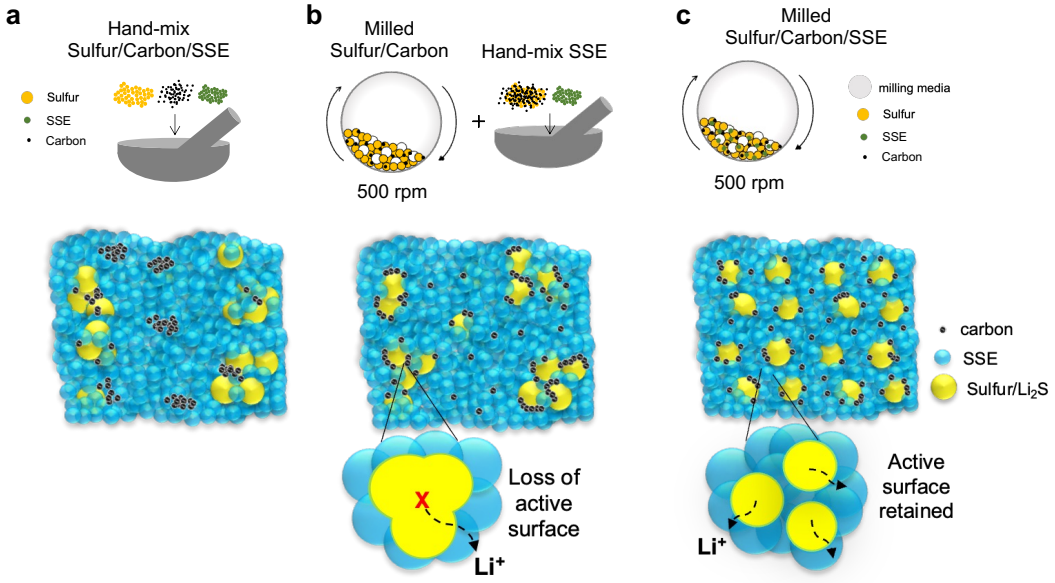

Supplemental Figure 2.1: Various cathode composite synthesis methods. Schematic illustrating the process of (a) hand-mixing all components, (b) milling carbon and sulfur followed by hand-mixing SSE and (c) single step milling of all components with their Expected distribution based on the 1st formation cycle.

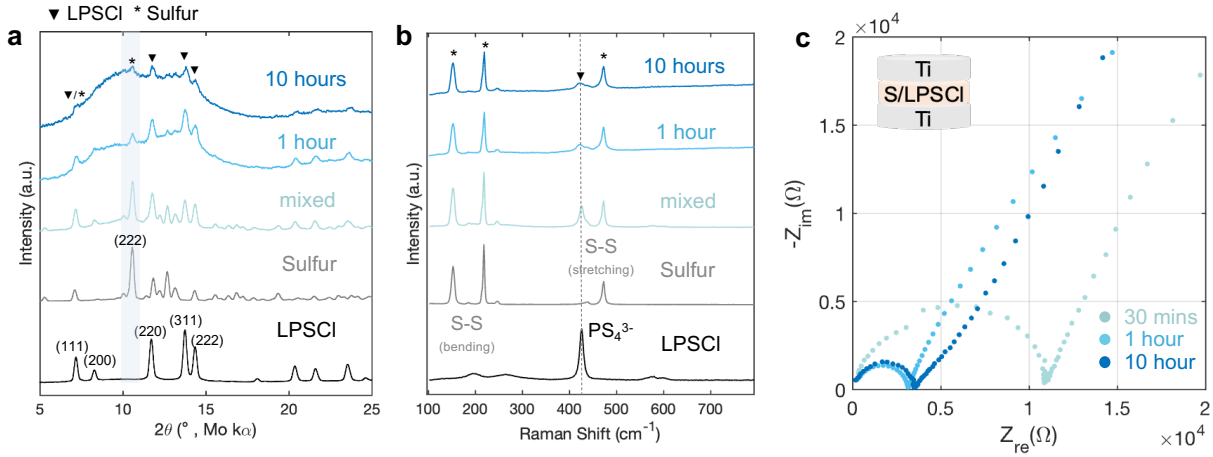

Supplemental Figure 2.2: Characterization of the sulfur composite after one-step synthesis without carbon. a) XRD spectra of S/LPSCl composite with increased milling durations. b) Raman spectra of composites shown in (a). c) Corresponding Nyquist plots of S/LPSCl composites with increasing milling durations.

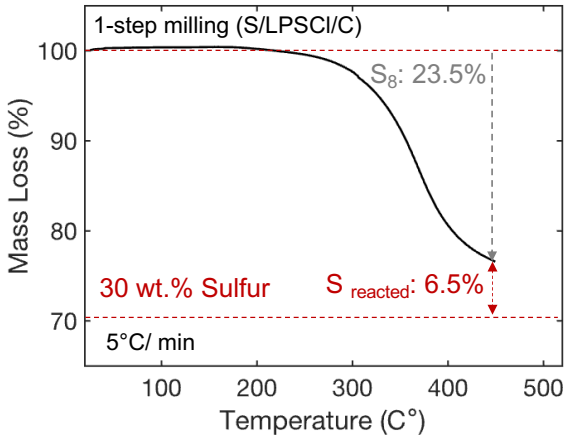

Supplemental Figure 2.3: Thermogravimetric analysis (TGA) of the sulfur composite with thermal rate of 5 C°/min.

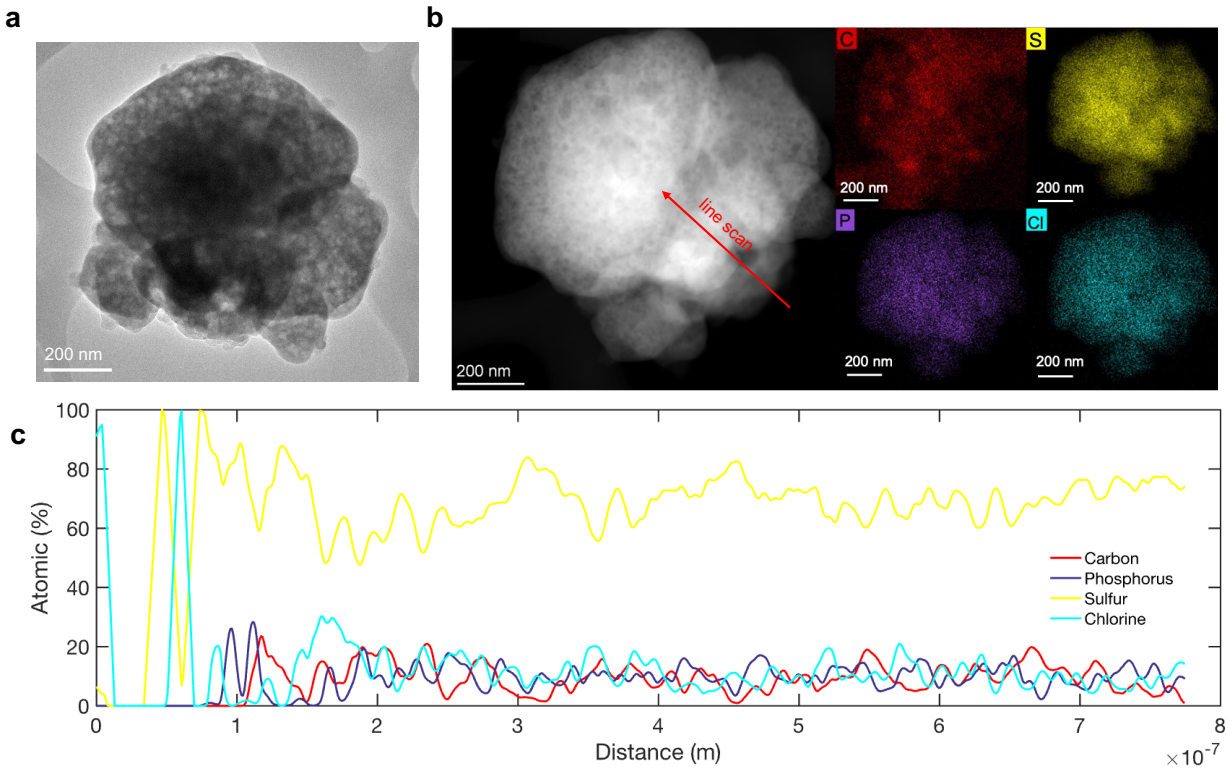

Supplemental Figure 2.4: Analysis of sulfur/LPSCl/C particle 1 after one-step synthesis. a) Low magnification TEM image. b) HAADF-STEM image of sulfur/LPSCl/C agglomerated particle 1 after synthesis with EDS hyperspectral imaging, and (c) line scan results.

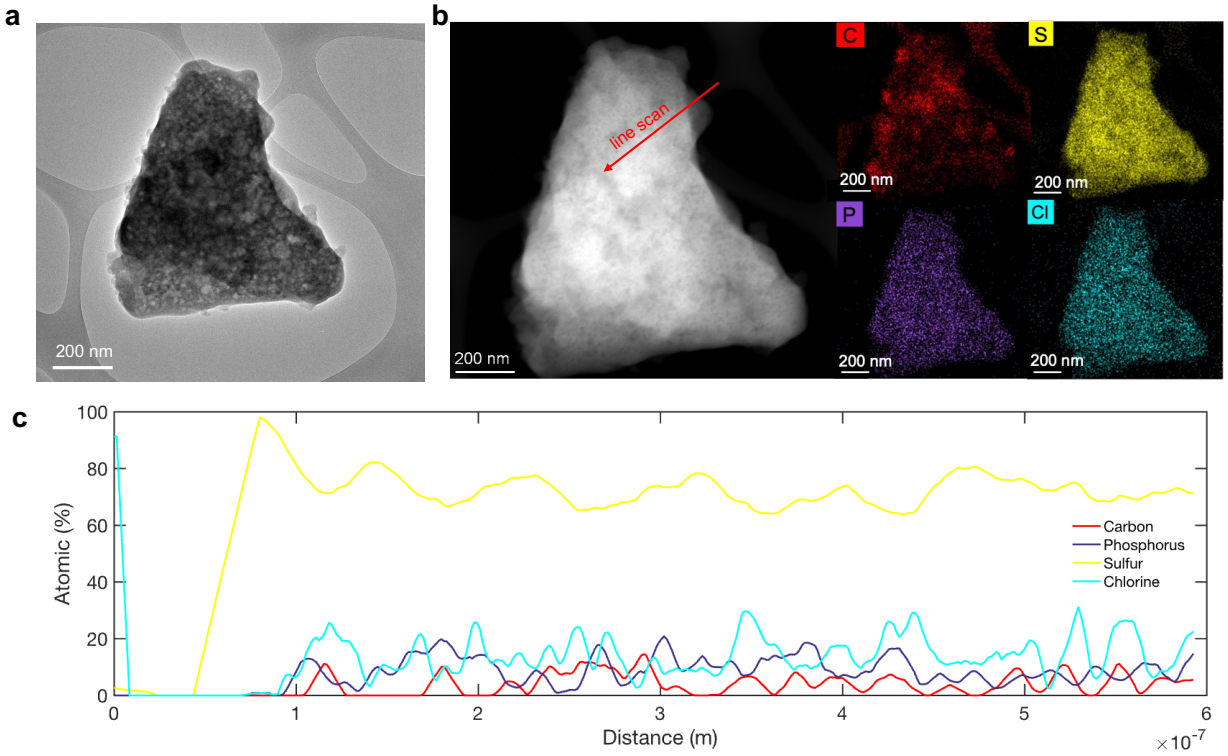

Supplemental Figure 2.5: Analysis of sulfur/LPSCl/C particle 2 after one-step synthesis. a) Low magnification TEM image. b) HAADF-STEM image of sulfur/LPSCl/C agglomerated particle 1 after synthesis with EDS hyperspectral imaging, and (c) line scan results.

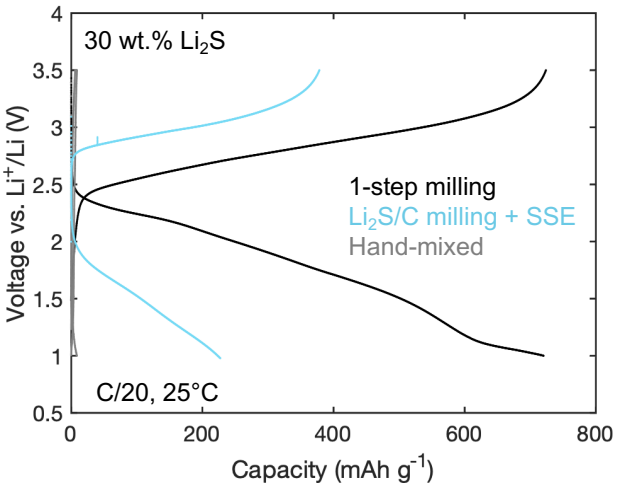

Supplemental Figure 2.6: Voltage profile of 1st formation cycle at C/20 of Li_2S cathode composites prepared by various methods.

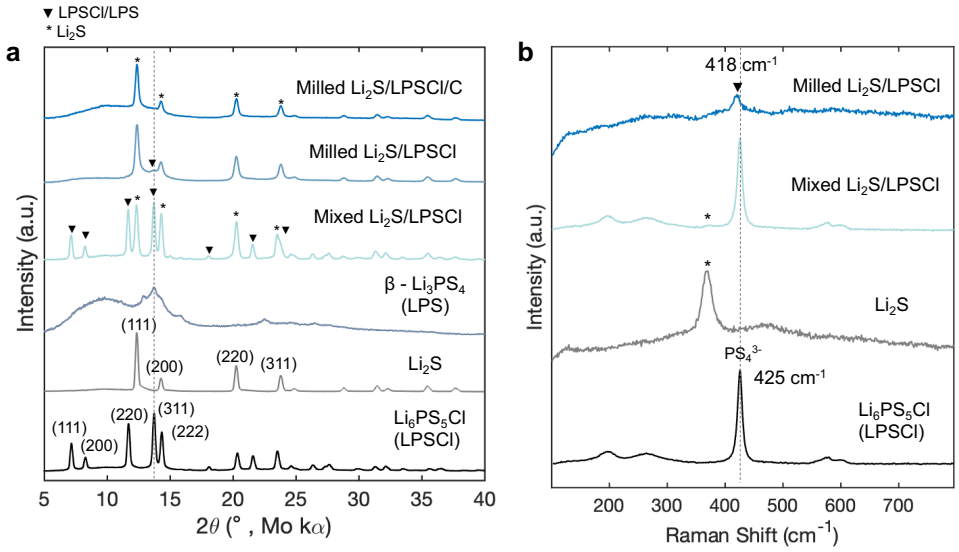

Supplemental Figure 2.7: Characterization of the Li_2S composite. a) X-ray diffraction of Li_2S/LPSCl/C composites comparing mixed, milled, and samples without carbon. b) Raman spectroscopy spectra comparing milled and mixed Li_2S/LPSCl composites without carbon.

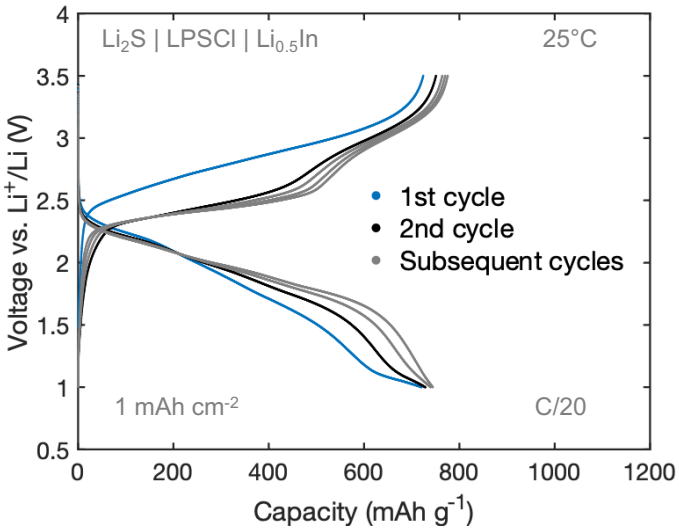

Supplemental Figure 2.8: Voltage profiles of Li_2S/LPSCl/$Li_{0.5}In$ cells evaluated at room temperature under C/20 cycling conditions.

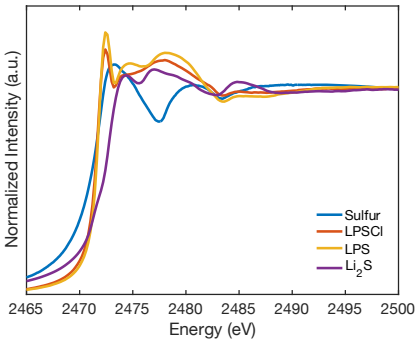

Supplemental Figure 2.9: X-ray absorption spectroscopy (XAS) spectra of Sulfur K-edge of reference species and expected redox products (i.e., Sulfur, LPSCl, LPS, and Li_2S).

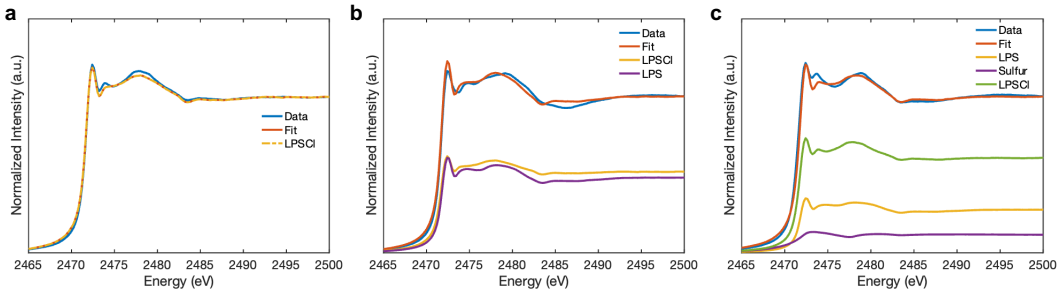

Supplemental Figure 2.10: Linear combination fitting of XAS spectra at Sulfur K-edge of the LPSCl system for the (a) Pristine state, (b) discharged state, and (c) charged (after 1 cycle) state.

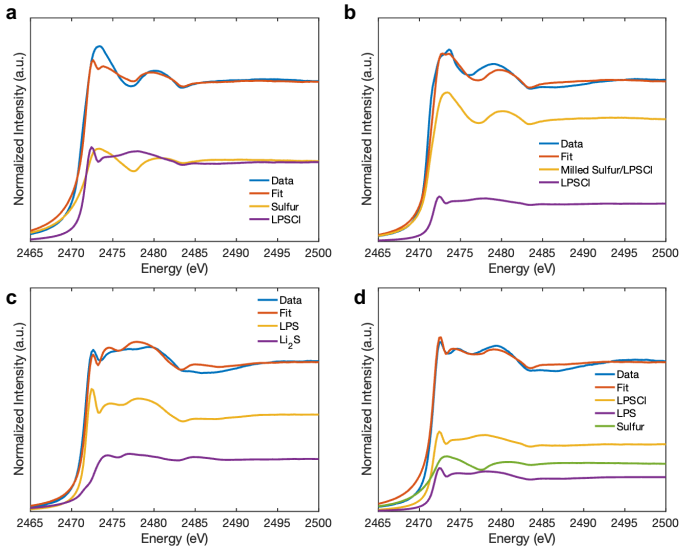

Supplemental Figure 2.11: Linear combination fitting of XAS spectra at Sulfur K-edge of the sulfur system. a) Milled Sulfur/LPSCl (without carbon). b) Pristine composite. c) Discharged composite. d) Charged composite (after 1 cycle) conditions.

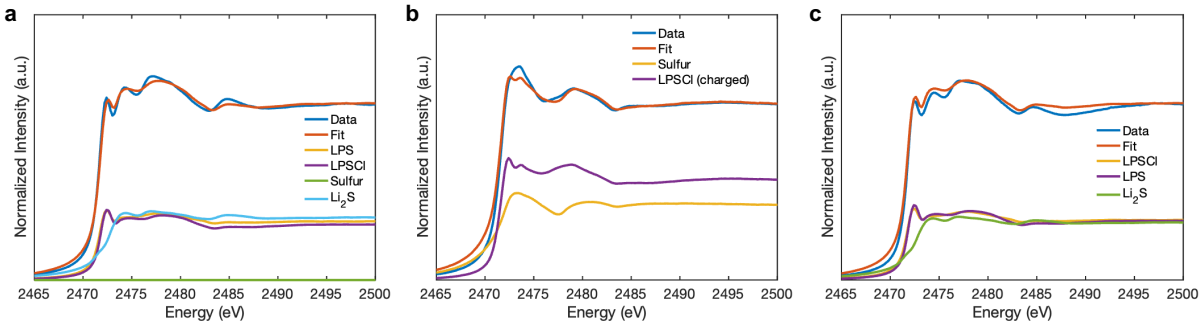

Supplemental Figure 2.12: Linear combination fitting of XAS spectra at Sulfur k-edge of the Li_2S system. (a) pristine composite and under (c) charged and (d) discharged (after 1 cycle) conditions.

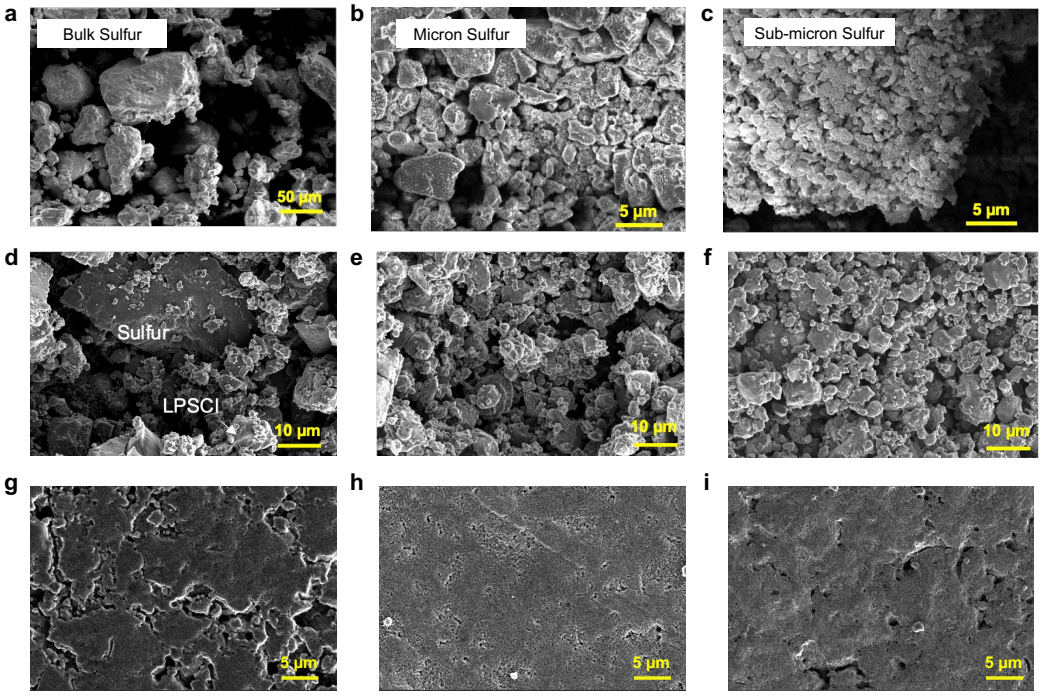

Supplemental Figure 2.13: Scanning electron microscopy (SEM) images of sulfur particle sizes and their composites. Powders of (a) bulk, (b) micron, and (c) sub-micron sulfur particles. Composite powder after synthesis of (d) bulk, (e) micron, and (f) sub-micron sulfur particles. Top view after composite fabrication for (g) bulk, (h) micron, and (i) sub-micron sulfur particles.

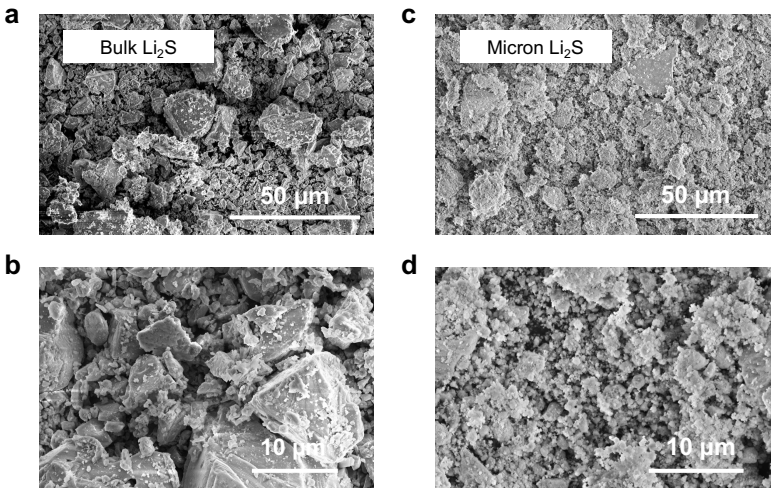

Supplemental Figure 2.14: SEM images of Li_2S powders. a) Low magnification and (b) high magnification of as received bulk Li_2S particles. c) Low magnification and (d) high magnification of micron Li_2S particles.

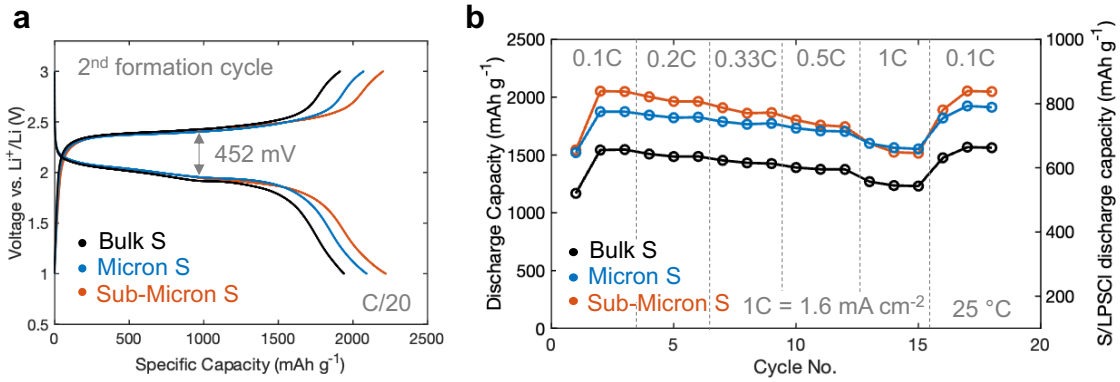

Supplemental Figure 2.15: Electrochemical results with differing sulfur particle sizes. a) Second formation cycle of bulk, micron, and sub-micron sulfur composites at C/20. b) Rate performance evaluation from 0.1C (0.16 mA cm^{-2}) to 1C at room temperature.

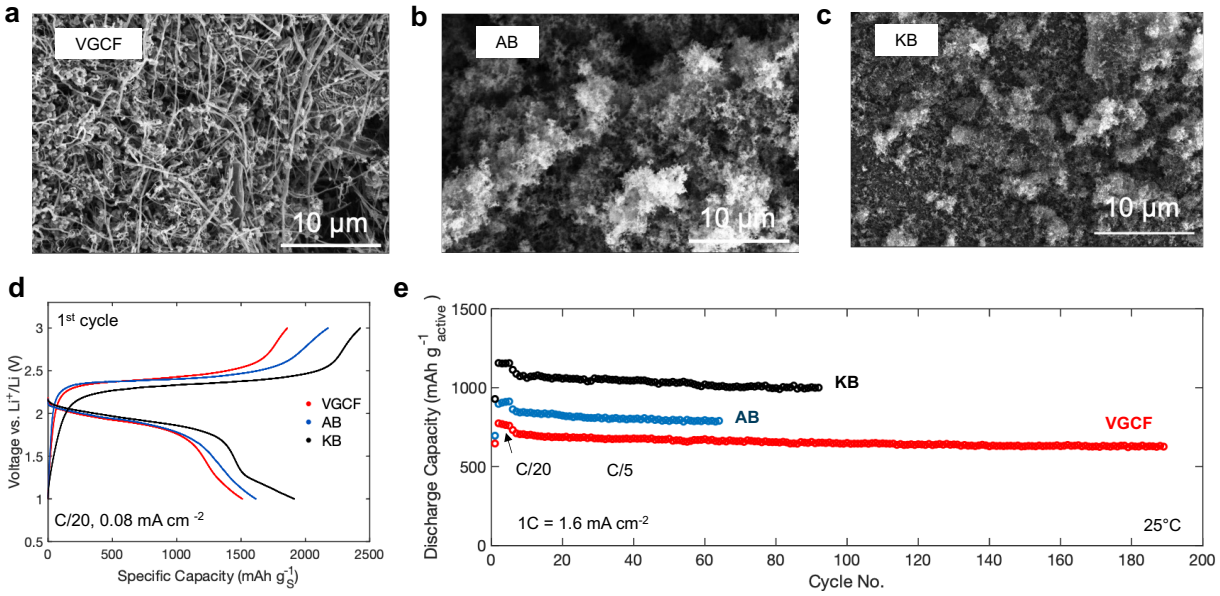

Supplemental Figure 2.16: Electrochemical evaluation of the micron sulfur cathode with various carbon types. SEM images of (a) vapor grown carbon fiber (VGCF), (b) acetylene black (AB) and (c) Ketjen black (KB, EC-600JD). d) First cycle voltage profile at C/20. e) Long term cycling performance at C/5.

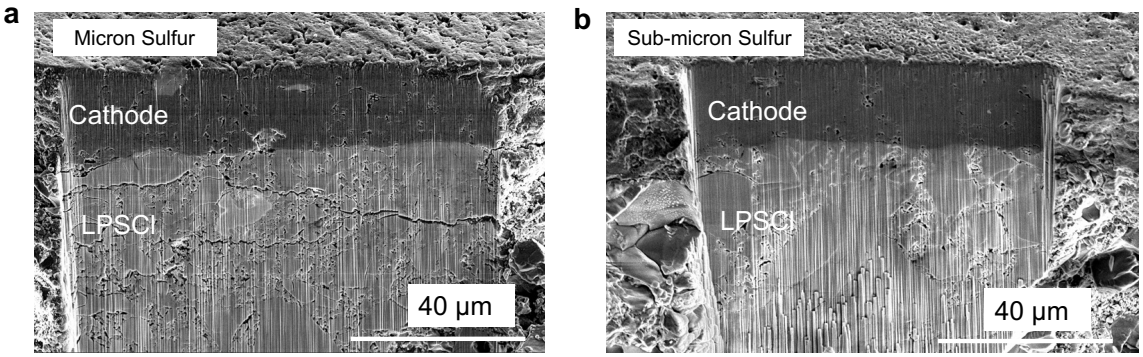

Supplemental Figure 2.17: Cross-sectional SEM images of sulfur cathode composites under cryogenic conditions. a) Micron sulfur cathode composite after fabrication. b) Sub-micron sulfur cathode composite after fabrication.

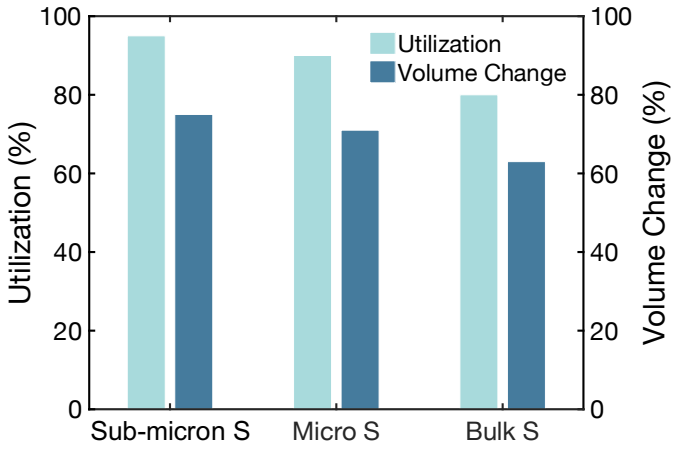

Supplemental Figure 2.18: Estimated volume expansion of sulfur particles based on % utilization obtained from first discharge capacities at C/20. This also considers the capacity contribution of LPSCl during the discharge process.

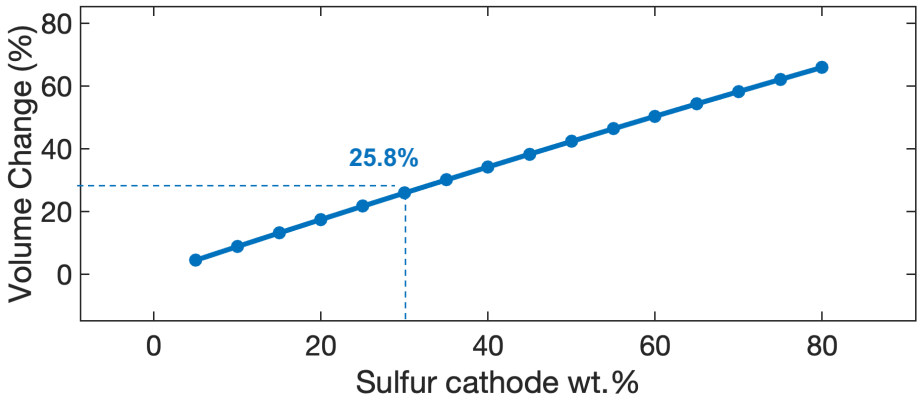

Supplemental Figure 2.19: Estimated volume change (%) of the cathode composite as a function of sulfur weight percent. Assuming only sulfur undergoes 80% volume change after complete lithiation.

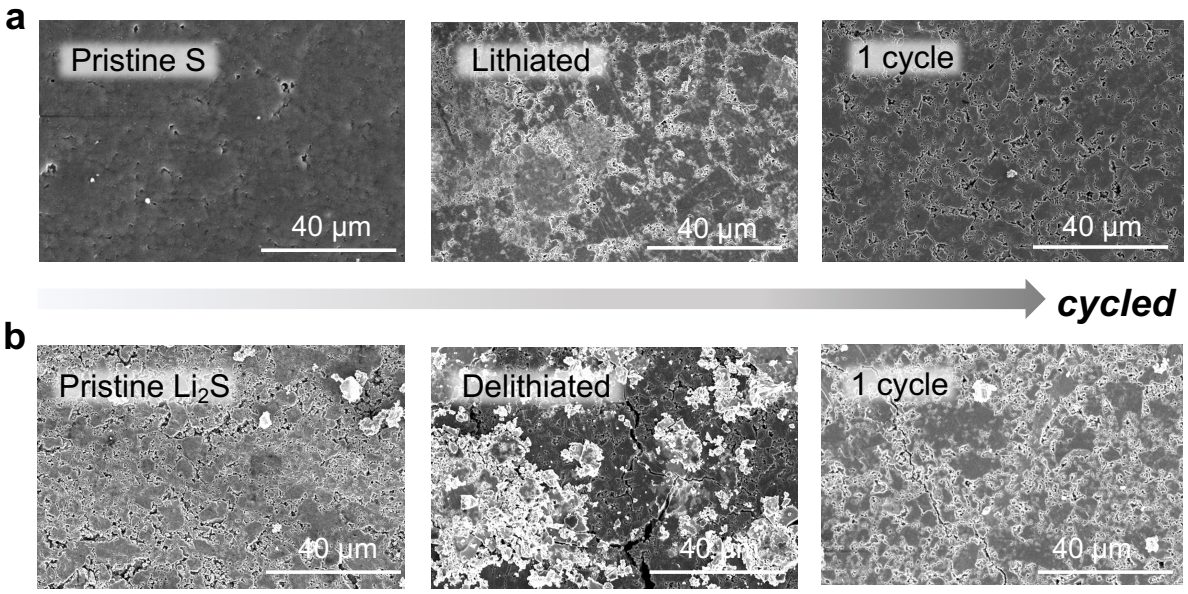

Supplemental Figure 2.20: Top surface images of Li-S cathodes at various states of charge. a) Sulfur cathode composite surface morphology with cycling. b) Li_2S cathode composite surface morphology with cycling.

Supplemental Table 2.1: Scanning transmission electron (STEM) microscopy elemental mapping results.

Particle 1

Z	Element	Family	Atomic Fraction (%)	Atomic Error (%)	Mass Fraction (%)	Mass Error (%)	Fit Error (%)
8	O	K	16.65	3.94	9.02	1.27	0.85
15	P	K	7.82	2.37	8.20	1.94	0.95
16	S	K	68.68	20.67	74.56	17.36	0.12
17	Cl	K	6.85	2.05	8.22	1.89	0.56

Particle 2

Z	Element	Family	Atomic Fraction (%)	Atomic Error (%)	Mass Fraction (%)	Mass Error (%)	Fit Error (%)
8	O	K	19.88	4.57	10.96	1.50	0.29
15	P	K	7.62	2.27	8.14	1.90	0.58
16	S	K	65.79	19.44	72.70	16.78	0.19
17	Cl	K	6.71	1.97	8.20	1.87	0.28

Supplemental Table 2.2: Sulfur K-edge XAS linear combination fitting results.

Composite	Sample	Species Wt.%				χ^2	R-factor
		Sulfur	LPSCl	LPS	Li_2S		
LPSCl/C	Pristine	0	100	0	0	0.03044	0.0005281
	Discharge	0	52.1	47.9	0	0.06229	0.0010326
	Charge	11.60	60.9	27.5	0	0.07749	0.0012868
S/LPSCl/C	Pristine	38.37	61.6	0	0	0.24154	0.0041802
	Discharge	0	0	64.6	35.4	0.12881	0.0568044
	Charge	32.0	45.1	22.9	0	0.05798	0.0219914
Li_2S/LPSCl/C	Pristine	0	33.2	31.2	35.6	0.04966	0.0008985
	Charge	45.4	37.6	16.99	0	0.09713	0.0407643
	Discharge	0	34.0	33.3	32.7	0.11070	0.0020389

Supplemental Table 2.3: Parameters used in FEM simulations.

Name	**Symbol**	**Value**
Young Modulus of S	E_S	17.8 GPa
Young Modulus of LPSCl	E_{SE}	22 GPa
Poisson ratio of S	υ_S	0.32
Poisson ratio of LPSCl	υ_{SE}	0.3
Density of S	ρ_S	2 $g.cm^{-3}$
Density of LPSCl	ρ_{SE}	1.6 $g.cm^{-3}$
Hygroscopic coefficient of S_{micro}	β_H	$22.5.10^{-3}$ $m^3.kg^{-1}$
Hygroscopic coefficient of $S_{sub\text{-}micro}$	β_H	24.10^{-3} $m^3.kg^{-1}$
Molar mass of Li	M_m	7.10^{-3} $kg.mol^{-1}$

Supplemental Table 2.4: Equations used in FEM simulations.

Name	**Symbol**
On external boundaries	$u = 0$
In the electrode	$\rho \frac{\partial^2 u}{\partial^2 t} = \nabla S + F_V$ $S = C : \epsilon_{el}$ $C = C(E, \upsilon)$ $\epsilon_{el} = \epsilon - \epsilon_{inel}$ $\epsilon_{inel} = \epsilon_{Hs}$ $\epsilon = \frac{1}{2}[(\nabla u)^T + \nabla u]$
Hygroscopic swelling in S particles	$\epsilon_{Hs} = \beta_H M_m C_{Li}$
Initial values	$u = 0$ $\frac{\partial u}{\partial t} = 0$

Supplemental Table 2.5: Values used for energy density calculations.

	Sulfur | Li Metal	**Sulfur | Li_2Si**	**Li_2S | 100% Silicon**	**Li_2S | Li Metal**	**Li_2S | Anode-free**
Nominal Voltage / V	1.7	1.7	1.4	1.7	1.7
Areal Capacity / mAh cm^{-2}	10	10	10	10	10
Cathode / %	30	30	30	30	30
NP ratio	1.2	1.2	1.2	1.2	-
Anode Capacity / mAh g^{-1}	3500	860 (experimental)	3500	3500	-
Anode Density / g cm^{-3}	0.5	-	2.3	0.5	-
Cathode Capacity / mAh g^{-1}	1600	1600	1000	1000	1000
Cathode Density / g cm^{-3}	2	2	1.66	1.66	1.66
SSE Thickness / µm	30	30	30	30	30
SSE Density / g cm^{-3}	1.6	1.6	1.6	1.6	1.6
SSE Relative Density / %	85	85	85	85	85
Cu Foil Thickness / µm	10	10	10	10	10
Cu Foil Density / g cm^{-3}	8.9	8.9	8.9	8.9	8.9
Al Foil Thickness / µm	10	10	10	10	10
Al Foil Density / g cm^{-3}	2.7	2.7	2.7	2.7	2.7
Binder ratio / %	1	1	1	1	1

Acknowledgements

Chapter 2, in full, has been submitted for publication and is currently under review. Cronk, Ashley; Wang, Xiaowei; Oh, Jin An Sam; Han, So-Yeon; Bai, Shuang; Ridley, Phillip; Chouchane, Mehdi; Huang, Chen-Jui; Cheng, Diyi; Deysher, Grayson; Yang, Hedi; Sayahpour, Baharak; Vicencio, Marta; Lee, Choonghyeon; Lee, Dongchan, Lee; Song, Min-Sang; Jang, Jihyun; Lee, Jeong Beom; Meng, Y. Shirley, Nature Energy, 2024, *Under Review*. The dissertation author was the primary investigator and author of this paper.

SUMMARY AND FUTURE PERSPECTIVE

Climate change has accelerated the decarbonization of our energy infrastructure and development of alternative and renewable energy sources. Since renewable sources are intermittent, these new infrastructures need to be complimented with energy storage such as batteries that can store and deliver energy when needed. Batteries are also proving to be fundamental for electrifying mobility technologies, where ideally these systems should be charged from renewable sources.

Decades of research have amounted to significant advancements in battery technology, specifically for ASSBs which have been increasing in popularity and demand due to their promise of higher energy densities and improved safety compared to their LIB counterparts. The studies presented in this dissertation mainly focus on the design principles for cathode materials, which have required new strategies to be implemented into ASSBs. This is due to resistive solid interfaces with limited ionic and electronic percolating networks. Therefore, factors like particle size, carbon morphologies, synthesis approaches, resulting cathode microstructure, SSE selection, SSE redox behavior, and electrochemically reversibility were explored. This was also complimented by modeling and finite element method analysis, which allowed a deeper understanding of how these factors govern electrochemical and mechanical behavior. Advancing cathode capabilities is imperative to achieve higher energy densities. Although, anode materials can influence energy density and cell performance, the cathode capacity and voltage dictate the maximum battery energy output. The results of this dissertation reinforce motivation to pursue ASSB architectures, however some challenges still exist for their commercialization in aspects of materials science and engineering.

In this work, sulfide-based SSEs, mainly LPSCl was investigated thoroughly, where its compatibility with both LFP and Li-S was evaluated. For the LZC case, chloride based LZC electrolyte was found to be a more suitable catholyte material. However, improvements in rate performance can be achieved with the discovery of higher ionically conductive SSEs that are also oxidatively stable. The ionic conductivity of LZC is near 1 mS cm $^{-2}$, with low electronic conductivity.[83] To be competitive to liquid LIBs, ionic conductivity above 10 mS cm $^{-1}$ is required. Oxyhalides are a promising class of SSEs which satisfy the ionic conductivity and electrochemical stability requirement from their amorphous mixed anion structure.[119,120] Beyond ionic conductivity, other SSE properties like deformability, hardness, and density are also critical. More deformable SSEs with lower hardness can absorb energies from the expansion and contraction of active materials and preserve these interfaces with cycling. Also, lower density SSEs are beneficial for energy density savings, which result in higher volume percentages of ionic networks compared to the cathode material[80]. Either new, or improvements in SSE properties, are necessary to advance practical ASSBs. For the Li-S cathode design presented in this work, bonding between the sulfur and sulfur atoms in the SSE improved interfacial contact to the SSE matrix and created an ionically conductive interphase. This interaction between cathodes and SSEs can be tuned to create beneficial properties and should be explored further with other SSE candidates and conversion chemistries. Another opportunity is the discovery of mixed conductor SSEs which conduct both ions and electrons. This has been demonstrated in few works[121,122], which could potentially improve the kinetics and lithium transport without requiring conductive agents like carbon within the cathode. This would decrease the amount of inactive or 'dead weight' within the cell, leading to improvements in energy density. Novel materials discovery will accelerate advancements in

battery technology. However, other factors like cost and manufacturing capabilities still need to be considered.

ASSBs still face challenges hindering their commercialization and manufacturability. Large stack pressures required to constrain electrode expansion and facilitate intimate contact of the solid materials require bulky or heavy pressure fixtures that ultimately decrease energy density of the system.[112] Efforts to reduce weight from cell components seem insignificant when comparing the mass contribution from the pressure fixture. This component is typically not included in energy density calculations but should be considered in the future. Usually, large pressures can be mitigated with higher temperature operation, increasing the ionic conductivity and transport kinetics of the SSE. New strategies like pressure matching between conversion electrodes demonstrated in this work, pre-deformed 3D solid-electrolyte structures[76], or isostatic pressure vessels[123] can facilitate acceptable performance at lower operating pressures. Highly deformable and elastic SSEs, low volume change materials, or volume change matching materials, can overcome this stack pressure challenge.

ASSBs are still a premature technology meaning that manufacturing capabilities are still under development. Manufacturing ASSBs require new or renovated infrastructure, requiring investment in both manufacturing equipment and training appropriate personnel. Large roll-to-roll fabrication processes that make scalable dry process electrodes under dry room conditions are currently under investigation. Main hurdles to accelerate the manufacturability of ASSBs include their dry room stability, as most SSEs degrade in ambient conditions. Sulfide SSEs hold some promise in their dry room compatibility as investigated in prior works.[29] Dry room compatibility studies are imperative to evaluate the production viability of new SSEs.

ASSBs will likely not be the ultimate fix for energy storage and will not replace every type of battery technology. Their advantages make them highly competitive compared to their LIB counterparts. However, like renewable energy sources, not one system will be applicable for every circumstance, which varies dependent on location, resources, and needs. The pros and cons of each system need to be considered for its use and application. Other battery systems will need to exist in parallel where hybrid systems can complement the strengths and weaknesses of each system. Due to their kinetic limitations, ASSBs will likely not be used for fast charge and discharge applications unless significant advancements in SSEs or anode/cathode coating and materials are realized. However, if ASSBs can overcome the high stack pressures and scale up challenges, it will become a dominant energy storage system for a wide array of electrification technologies which include electric vehicles, grid storage, potentially electrified aircrafts, and portable electronics. Future research should focus on materials discovery, novel engineering approaches, scale up, electrode composite design and optimization, multi-scale physics-based modeling, and end of life impacts like recycling of these battery materials.

REFERENCES

1. Zubi, G.; Dufo-López, R.; Carvalho, M.; Pasaoglu, G. The lithium-ion battery: State of the art and future perspectives. Renewable and Sustainable Energy Reviews. 2018, vol. 89 292–308, DOI: 10.1016/j.rser.2018.03.002

2. Stampatori, D.; Raimondi, P. -P.; Noussan, M. Li-ion batteries: A review of a key technology for transport decarbonization. Energies (Basel). 2020, 13 (10) 2638, DOI: 10.3390/ en13102638

3. Olivetti, E.-A.; Ceder, G.; Gaustad, G.-G.; Fu, X. Lithium-Ion Battery Supply Chain Considerations: Analysis of Potential Bottlenecks in Critical Metals. Joule. 2017, vol. 1 229–243, DOI: 10.1016/j.joule.2017.08.019

4. Halm, I. Surging commodity prices could impact the growth of the EV sector. Mining Technology, 2022. https://www.mining-technology.com/analysis/commodity-prices-ev-sector-growth/. Accessed 31 May 2022.

5. Murdock, B.-E.; Toghill, K. E.; Tapia-Ruiz, N. A Perspective on the Sustainability of Cathode Materials used in Lithium-Ion Batteries. Advanced Energy Materials. 2021, 11, DOI: 10.1002/aenm.202102028

6. Padhi, A.-K.; Nanjundaswamy, K.-S.; Goodenough, J.-B. Phospho-olivines as Positive-Electrode Materials for Rechargeable Lithium Batteries. J. Electrochem. Soc. 1997, vol. 144, 1188-1194

7. Coppola, G.; Baker R.-D. Tesla Shifting to Cheaper Battery Chemistry Tried in China. Bloomberg US Edition. 2021. https://www.bloomberg.com/news/articles/2021-10-20/tesla-shifting-to-cheaper-battery-chemistry-tried-in-china/. Accessed 5 June 2022.

8. Kolodny, L. Rivian will follow Tesla and change the type of battery cells it uses in standard packs. CNBC. 2022. https://www.cnbc.com/2022/03/10/rivian-changing-battery-cells-to-lfp-following-tesla-and-high-nickel.html. Accessed 5 June 2022.

9. BloombergNEF. Lithium-Ion Batteries: 2021 State of the Industry Analysis, Long-Term Energy Storage Outlook, Long-Term Electric Vehicle Outlook and 2020 Lithium-Ion Battery Price Survey. 2021. https://about.newenergyfinance.com/electric-vehicle-outlook/. Accessed 5 June 2022.

10. International Energy Agency. Global EV Outlook 2022: Securing supplies for an electric future. 2022. https://www.iea.org/reports/global-ev-outlook-2022/. Accessed 5 June 2022.

11. Hu, J.; Huang, W.; Yang, L.; Pan, F. Structure and performance of the LiFePO4 cathode material: From the bulk to the surface. Nanoscale. 2020, vol. 12, 15036–15044, DOI: 10.1039/d0nr03776a

12. Hess, M.; Sasaki, T.; Villevieille, C.; Novák, P. Combined operando X-ray diffraction-electrochemical impedance spectroscopy detecting solid solution reactions of LiFePO4 in batteries. Nat Commun. 2015, 6, 8169, DOI: 10.1038/ncomms9169

13. Feng, X.; Ouyang, M.; Liu, X.; Lu, L.; Xia, Y.; He, X. Thermal runaway mechanism of lithium-ion battery for electric vehicles: A review. Energy Storage Materials. 2018, 10, 246–267 DOI: 10.1016/j.ensm.2017.05.013

14. Oh, D.-Y.; Nam, Y.-J.; Park, K.-H.; Jung, S.-H.; Cho, S.-J.; Kim, Y.-K.; Lee, Y.-G.; Lee, S.-Y.; Jung, Y.-S. Excellent Compatibility of Solvate Ionic Liquids with Sulfide Solid Electrolytes: Toward Favorable Ionic Contacts in Bulk-Type All-Solid-State Lithium-Ion Batteries. Adv Energy Mater. 2015, 5, 1500865, DOI: 10.1002/aenm.201500865

15. Yan, X.; Li, Z.; Wen, Z.; Han, W. Li/Li7La3Zr2O12/LiFePO4 all-solid-state battery with ultrathin nanoscale solid electrolyte. Journal of Physical Chemistry C. 2017, 121, 1431–1435.

16. Wang, Z.; Tan, R.; Wang, H.; Yang, L.; Hu, J.; Chen, H.; Pan, F. A Metal–Organic-Framework-Based Electrolyte with Nanowetted Interfaces for High-Energy-Density Solid-State Lithium Battery. Advanced Materials. 2018, 30, 1704436, DOI: 10.1002/adma.201704436

17. Ma, C.; Dai, K.; Hou, H.; Ji, K.; Chen, L.; Ivey, D.; Wei, W. High Ion-Conducting Solid-State Composite Electrolytes with Carbon Quantum Dot Nanofillers. Advanced Science. 2018, 5, 1700996.

18. Zeng, H.; Ji, X.; Tsai, F.; Zhang, Q.; Jiang, T.; Li, R.; Shi, H.; Luan, S.; Shi, D. Enhanced cycling performance for all-solid-state lithium-ion battery with LiFePO4 composite cathode encapsulated by poly (ethylene glycol) (PEG) based polymer electrolyte. Solid State Ionics. 2018, 320, 92–99.

19. Xu, H.; Chien, P.; Shi, J.; Li, Y.; Wu, N.; Liu, Y.; Hu, Y.; Goodenough, J. High-performance all-solid-state batteries enabled by salt bonding to perovskite in poly(ethylene oxide). Proc Natl Acad Sci U S A. 2019, 116, 18815–18821.

20. Wang, S.; Li, S.; Wei, B.; Lu, X. Interfacial Engineering at Cathode/LATP Interface for High-Performance Solid-State Batteries. J Electrochem Soc. 2020, 167, 100528.

21. Yang, C.; Wu, Q.; Xie, W.; Zhang, X.; Brozena A.; Zheng, J.; Garaga, M.; Ko, B.; Mao, Y.; He, S.; Gao, Y.; Wang, P.; Tyagi, M.; Jiao, F.; Briber, R.; Albertus, P.; Wang, C.; Greenbaum, S.; Hu, Y.; Isogai, A.; Winter, M.; Xu, K.; Qi, Y.; Hu, L. Copper-

coordinated cellulose ion conductors for solid-state batteries. Nature. 2021, 598, 590–596.

22. Zagórski, J.; Silván, B.; Saurel, D.; Aguesse, F.; Llordés, A. Importance of Composite Electrolyte Processing to Improve the Kinetics and Energy Density of Li Metal Solid-State Batteries. ACS Appl Energy Mater. 2020, 3, 8344–8355.

23. Erabhoina, H.; Thelakkat, M. Tuning of composition and morphology of LiFePO4 cathode for applications in all solid-state lithium metal batteries. Sci Rep. 2020. 12, 1.

24. Li, J.; Qi, J.; Jin, F.; Zhang, L.; Tang, L.; Huang, R.; Xu, J.; Chen, H.; Liu, M.; Qiu, Y.; Cooper, A.; Shen, Y.; Chen, L. Room temperature all-solid-state lithium batteries based on a soluble organic cage ionic conductor. Nat Commun. 2022. 13 (1), DOI: 10.1038/41467-022-29743-1

25. Chen, H.; Yu, L.; Cao, X.; Yang, Q.; Liu, Y.; Wei, Y.; Zeng, J.; Zhong, L.; Qiu, Y. The multicomponent synergistic effect of a hierarchical Li0.485La0.505TiO3 solid-state electrolyte for dendrite-free lithium-metal batteries. Nanoscale. 2022, 14, 7766–7777.

26. Rosenbach, D.; Krimalowski, A.; Erabhoina, H.; Thelakkat, M. Solid polymer electrolytes from polyesters with diester sidechains for lithium metal batteries. J Mater Chem A Mater. 2022, DOI:10.1039/d2ta00800a.

27. Tatsumisago, M.; Nagao, M.; Hayashi, A. Recent development of sulfide solid electrolytes and interfacial modification for all-solid-state rechargeable lithium batteries. Journal of Asian Ceramic Societies. 2013,1 17–25, DOI: 10.1016/j.jascer.2013.03.005

28. Bai, X.; Duan, Y.; Zhuang, W.; Yang, R.; Wang, J. Research progress in Li-argyrodite-based solid-state electrolytes. Journal of Materials Chemistry A. 2020, 8, 25663–25686 DOI: 10.1039/d0ta08472g

29. Chen, Y.-T.; Marple, M.; Tan, D.; Ham, S.; Sayahpour, B.; Li, W.; Yang, H.; Lee, J.; Hah, H.; Wu, E.; Doux, J.; Jang, J.; Ridley, P.; Cronk, A.; Deysher, G.; Chen, Z.; Meng, Y. Investigating dry room compatibility of sulfide solid-state electrolytes for scalable manufacturing. J Mater Chem A Mater. 2022, 10, 7155–7164

30. Byeon, Y.-W.; Kim, H. Review on Interface and Interphase Issues in Sulfide Solid-State Electrolytes for All-Solid-State Li-Metal Batteries. Electrochem. 2021, 2, 452–471.

31. Wu, E.-A.; Jo, C.; Tan, D.-H.-S.; Zhang, M.; Doux, J.; Chen, Y.; Deysher, G.; Meng, Y.-S. A Facile, Dry-Processed Lithium Borate-Based Cathode Coating for Improved All-Solid-State Battery Performance. J Electrochem Soc. 2020, 167, 130516.

32. Kitsche, D.; Tang, Y.; Ma, Y.; Goonetilleke, D.; Sann, J.; Walther, F.; Bianchini, M.; Janek, J.; Brezesinski. High Performance All-Solid-State Batteries with a Ni-Rich NCM

Cathode Coated by Atomic Layer Deposition and Lithium Thiophosphate Solid Electrolyte. ACS Appl Energy Mater. 2021, 4, 7338–7345.

33. Culver, S. P.; Koerver, R.; Zeier, W.-G.; Janek, J. On the Functionality of Coatings for Cathode Active Materials in Thiophosphate-Based All-Solid-State Batteries. Advanced Energy Materials. 2019, 9. DOI:10.1002/aenm.201900626.

34. Kwak, H.-W.; Park, Y.-J. Cathode coating using LiInO2-LiI composite for stable sulfide-based all-solid-state batteries. Sci Rep. 2019, 9, 8099, DOI: 10.1038/s41598-019-44629-x

35. Tan, D.-H.-S.; Banerjee, A.; Chen, Z; Meng, Y.-S. From nanoscale interface characterization to sustainable energy storage using all-solid-state batteries. Nat Nanotechnol. 2020. 15, 170–180.

36. Li, X. et al. Progress and perspectives on halide lithium conductors for all-solid-state lithium batteries. Energy and Environmental Science. 2020, 13, 1429–1461, DO:1039/c9ee03828k

37. Kato, A.;Yamamoto, M.; Sakuda, A.; Hayashi, A.; Tatsumisago, M. Mechanical Properties of Li2S-P2S5 Glasses with Lithium Halides and Application in All-Solid-State Batteries. ACS Appl Energy Mater. 2018, 1, 1002–1007.

38. Asano, T.; Sakai, A.; Ouchi, S.; Sakaida, M.; Miyazaki, A.; Hasegawa, S. Solid Halide Electrolytes with High Lithium-Ion Conductivity for Application in 4 V Class Bulk-Type All-Solid-State Batteries. Advanced Materials. 2018, 30, 1803075.

39. Li, X.; Liang, J.; Luo, J.; Norouzi Banis, M.; Wang, C.; Li, W.; Deng, S.; Yu, C.; Zhao, F.; Hu, Y.; Sham, T.; Zhang, L.; Zhao, S.; Lu, S.; Huang, H.; Li, R.; Adair, K.; Sun, X. Air-stable Li3InCl6 electrolyte with high voltage compatibility for all-solid-state batteries. Energy Environ Sci. 2019, 12, 2665–2671.

40. Kwak, H.; Han, D.; Lyoo, J.; Park, J.; Jung, S.; Han, Y.; Kwon, G.; Kim, H.; Hong, S.; Nam, K.; Jung, Y.-S. New Cost-Effective Halide Solid Electrolytes for All-Solid-State Batteries: Mechanochemically Prepared Fe3+-Substituted Li2ZrCl6. Adv Energy Mater. 2021, 11, 2003190.

41. Kim, S.-Y.; Kaup, K.; Park, K.-H.; Assoud, A.; Zhou, L.; Liu, J.; Wu, X.; Nazar, L.-F. Lithium Ytterbium-Based Halide Solid Electrolytes for High Voltage All-Solid-State Batteries. ACS Mater Lett. 2021, 3, 930–938.

42. Park, K.-H.; Kavish, K.; Assoud, A.; Zhang, Q.; Wu, X.; Nazar, L.-F. High-Voltage Superionic Halide Solid Electrolytes for All-Solid-State Li-Ion Batteries. ACS Energy Lett. 2020, 533–539, DOI:10.1021/acsenergylett.9b02599.

43. Cao, D.; Zhang, Y.; Nolan, A.; Sun, X.; Liu, C.; Sheng, J.; Mo, Y.; Wang, Y.; Zhu, H. Stable Thiophosphate-Based All-Solid-State Lithium Batteries through Conformally Interfacial Nanocoating. Nano Lett. 2020, 20, 1483–1490.

44. Wang, K.; Ren, Q.; Gu, Z.; Duan, C.; Wang, J.; Zhu, F.; Fu, Y.; Hao, J.; Zhu, J.; He, L.; et al. A cost-effective and humidity tolerant chloride solid electrolyte for lithium batteries. Nat. Commun. 2021. 12, 4410, DOI: 10.1038/s41467-021-24697-2

45. Banerjee, A.; Wang, X.; Fang, C.; Wu, E.-A.; Meng, Y.-S. Interfaces and Interphases in All-Solid-State Batteries with Inorganic Solid Electrolytes. Chemical Reviews. 2020, 120, 6878–6933, DOI: 10.1021/acs.chemrev.0c00101

46. Doux, J.-M., Yang, Y.; Tan, D.-H.-S.; Nguyen, H.; Wu, E.-A.; Wang, X.; Banerjee, A.; Meng, Y.-S. Pressure effects on sulfide electrolytes for all solid-state batteries. J Mater Chem A Mater. 2020. 8, 5049–5055.

47. Zhang, W.; Leichtweiß, T.; Culver, S.-P.; Koerver, R.; Das, D.; Weber, D.-A.; Zeier, W.-G.; Janek, J. The Detrimental Effects of Carbon Additives in Li10GeP2S12-Based Solid-State Batteries. ACS Appl Mater Interfaces. 2017, 9, 35888–35896

48. Auvergniot, J.; Cassel, A.; Ledeuil, J.; Viallet, V.; Seznec, V.; Dedryvere, R. Interface Stability of Argyrodite Li6PS5Cl toward LiCoO2, LiNi1/3Co1/3Mn1/3O2, and LiMn2O4 in Bulk All-Solid-State Batteries. Chemistry of Materials. 2017, 29, 3883–3890

49. Wu, J.; Krishna, G.; Dathar, P.; Sun, C.; Theivanayagam, M.-G.; Applestone, D.; Dylla, A.-G.; Manthiram, A.; Henkelman, G.; Goodenough, J.-B.; Stevenson, K. In situ Raman spectroscopy of LiFePO4: Size and morphology dependence during charge and self-discharge. Nanotechnology. 2013, 24, 42.

50. Okubo, M.; Asakura, D.; Mizuno, Y.; Kim, J.; Mizokawa, T.; Kudo, T.; Honma, I. Switching redox-active sites by valence tautomerism in prussian blue analogues AxMny[Fe(CN)6]· n H2O (A: K, Rb): Robust frameworks for reversible Li storage. Journal of Physical Chemistry Letters. 2010, 1, 2063–2071.

51. Mei, B.-A.; Munteshari, O.; Lau, J.; Dunn, B.; Pilon, L. Physical Interpretations of Nyquist Plots for EDLC Electrodes and Devices. Journal of Physical Chemistry C. 2018, 122, 194–206.

52. Asano, T.; Yubuchi, S.; Sakuda, A.; Hayashi, A.; Tatsumisago, M. Electronic and Ionic Conductivities of LiNi1/3Mn1/3Co1/3O2 -Li3PS4 Positive Composite Electrodes for All-Solid-State Lithium Batteries. J Electrochem Soc. 2017, 164, A3960–A3963.

53. Chen, Y.; Duquesnoy, M.; Tan, D.-H.-S.; Doux, J.-M.; Yang, H.; Deysher, G.; Ridley, P.; Franco, A.-A.; Meng, Y.-S.; Chen, Z. Fabrication of High-Quality Thin Solid-State

Electrolyte Films Assisted by Machine Learning. ACS Energy Lett. 2021, 6, 4, 1639-1648. DOI: 10.1021/acsenergylett.1c00332

54. Toby, B.-H.; Dreele, R.-B. GSAS-II: the genesis of a modern open-source all-purpose crystallography software package. Journal of Applied Chemistry. 2013, 46, 544-549.

55. Fairley, N.; Fernandez, V.; Richard-Plouet, M.; Guillot-Deudon, C.; Walton, J.; Smith, E.; Flahaut, D.; Greiner, M.; Biesinger, M.; Tougaard, S.; et al. Systematic and collaborative approach to problem solving using X-ray photoelectron microscopy. *Appl. Surf. Sci.* 2021, 5, 100112. DOI: 10.1016/j.apsadv.2021.100112

56. A. Marjolin. Lithium-ion battery capacity to grow steadily to 2030. *S&P Global Market Intelligence* (2023).

57. B. A. Adu-Gyamfi, C. Good, Electric aviation: A review of concepts and enabling technologies. *Transportation Engineering*, **9**, 100134, (2022).

58. D. A. Dornbusch, R. P. Viggiano, J. W. Connell, Y. Lin, V. F. Lvovich, Practical considerations in designing solid state Li-S cells for electric aviation. *Electrochim Acta*, **403** (2022).

59. A. Manthiram, Y. Fu, Y. S. Su, Challenges and prospects of lithium-sulfur batteries. *Acc Chem Res* **46**, 1125–1134 (2013).

60. J. Sun, T. Wang, Y. Gao, Z. Pan, R. Hu, J. Wang, Will lithium-sulfur batteries be the next beyond-lithium-ion batteries and even much better? *InfoMat*, DOI: 10.1002/inf2.12359 (2022).

61. J. R. Akridge, Y. V. Mikhaylik, N. White, Li/S fundamental chemistry and application to high-performance rechargeable batteries. *Solid State Ionics*, **175**, 243-245 (2004).

62. Ren, W., Ma, W., Zhang, S. Tang, B. Recent advances in shuttle effect inhibition for lithium sulfur batteries. *Energy Storage Materials*, **23,** 707–732 (2019).

63. S. Ohno, W. G. Zeier. Toward Practical Solid-State Lithium-Sulfur Batteries: Challenges and Perspectives. *Acc Mater Res.,* **2**, 869–880 (2021).

64. A. Manthiram, Y. Fu, S. H. Chung, S. Zu, Y.S. Su. Rechargeable lithium-sulfur batteries. *Chemical Reviews* vol. 114 11751–11787, (2014).

65. J.A., Lewis, J. Tippens, F. J. Q., Cortes, M.T., McDowell. Chemo-Mechanical Challenges in Solid-State Batteries. *Trends in Chemistry* vol. 1 845–857 (2019).

66. M. Chen, S. Adams, High performance all-solid-state lithium/sulfur batteries using lithium argyrodite electrolyte. *Journal of Solid-State Electrochemistry*, **19**, 697–702 (2015).

67. S. Kinoshita, K. Okuda, N. Machida, M. Naito, T. Sigematsu, All-solid-state lithium battery with sulfur/carbon composites as positive electrode materials. *Solid State Ion.,* **256**, 97–102 (2014).

68. C. Yu, L. van Eijck, S. Ganapathy, M. Wagemaker, Synthesis, structure, and electrochemical performance of the argyrodite Li_6PS_5Cl solid electrolyte for Li-ion solid state batteries. *Electrochim Acta*., **215**, 93–99 (2016).

69. X. Zhu, W. Jiang, S. Zhao, R. Huang, M. Ling, C. Liang, L. Wang, Exploring the concordant solid-state electrolytes for all-solid-state lithium-sulfur batteries. *Nano Energy*, **96** (2022).

70. H. Kim, H. N. Choi, J. Y. Hwang, C. S. Yoon, Y. K. Sun, Tailoring the Interface between Sulfur and Sulfide Solid Electrolyte for High-Areal-Capacity All-Solid-State Lithium-Sulfur Batteries. *ACS Energy Lett*., 3971–3979 (2023).

71. S. Wang, Y. Zhang, X. Zhang, T. Liu, Y. H. Lin, Y. Shen, L. Li, C. W. Nan, High-Conductivity Argyrodite Li_6PS_5Cl Solid Electrolytes Prepared via Optimized Sintering Processes for All-Solid-State Lithium-Sulfur Batteries. *ACS Appl Mater Interfaces*, **10**, 42279–42285 (2018).

72. Y. Zhang, T. Liu, Q. Zhang, X. Zhang, S. Wang, X. Wang, L. Li, L. Z. Fan, C. W. Nan, Y. Shen, High-performance all-solid-state lithium-sulfur batteries with sulfur/carbon nano-hybrids in a composite cathode. *J Mater Chem A Mater*, **6**, 23345–23356 (2018).

73. X. Yao, N. Huang, F. Han, Q. Zhang, H. Wan, J. P. Mwizerwa, C. Wang, X. Xu, High-Performance All-Solid-State Lithium–Sulfur Batteries Enabled by Amorphous Sulfur-Coated Reduced Graphene Oxide Cathodes. *Adv. Energy Mater*, **7** (2017).

74. A. S. Alzahrani, M. Otaki, D. Wang, Y. Gao, T. S. Arthur, S. Liu, D. Wang, Confining Sulfur in Porous Carbon by Vapor Deposition to Achieve High-Performance Cathode for All-Solid-State Lithium-Sulfur Batteries. *ACS Energy Lett*., **6**, 413–418 (2021).

75. J. Zhou, M. L. Holekevi Chandrappa, S. Tan, S. Wang, C. Wu, H. Nguyen, C. Wang, H. Liu, S. Yu, Q. R. S. Miller, G. Hyun, J. Holoubek, J. Hong, Y. Xiao, C. Soulen, Z. Fan, E. E. Fullerton, C. J. Brooks, C. Wang, R. J. Clément, Y. Yao, E. Hu, S. P. Ong, P. Liu, Healable and conductive sulfur iodide for solid-state Li–S batteries. *Nature* **627**, 301–305 (2024).

76. K. Fu, Y. Gong, G. T. Hitz, D. W. McOwen, Y. Li, S. Xu, Y. Wen, L. Zhang, C. Wang, G. Pastel, J. Dai, B. Liu, H. Xie, Y. Yao, E. D. Wachsman, L. Hu, Three-dimensional bilayer garnet solid electrolyte based high energy density lithium metal-sulfur batteries. *Energy Environ. Sci.,* **10**, 1568–1575 (2017).

77. H. Yang, L. Wang, C. Geng, Y. Zhao, Q. Li, X. Jiang, Z. Tian, M. Wang, C. Jiang, Z. Sun, B. Cui, Y. B. He, W. Chen, W. Lv, Q. H. Yang, Catalytic Solid-State Sulfur Conversion Confined in Micropores toward Superhigh Coulombic Efficiency Lithium-Sulfur Batteries. *Adv Energy Mater*, doi: 10.1002/aenm.202400249 (2024).

78. Y. Liu, X. Meng, Z. Wang, J. Qiu, A Li_2S-based all-solid-state battery with high energy and superior safety. *Sci. Adv*., **8**, eabl8390 (2022).

79. X. Zhu, L. Wang, Z. Bai, J. Lu, T. Wu, Sulfide-Based All-Solid-State Lithium–Sulfur Batteries: Challenges and Perspectives. *Nanomicro. Lett.,* 15 (2023).

80. D. Wang, L. J. Jhang, R. Kou, M. Liao, S. Zheng, H. Jiang, P. Shi, G. X. Li, K. Meng, D. Wang, Realizing high-capacity all-solid-state lithium-sulfur batteries using a low-density inorganic solid-state electrolyte. *Nat Commun*., **14** (2023).

81. D. H. S. Tan, E. A. Wu, H. Nguyen, Z. Chen, M. A. T. Marple, J. M. Doux, X. Wang, H. Yang, A. Banerjee, Y. S. Meng, Elucidating Reversible Electrochemical Redox of Li_6PS_5Cl Solid Electrolyte. *ACS Energy Lett.*, 2418–2427 (2019).

82. J. Jang, Y. T. Chen, G. Deysher, D. Cheng, S. Y. Ham, A. Cronk, P. Ridley, H. Yang, B. Sayahpour, B. Han, W. Li, W. Yao, E. A. Wu, J. M. Doux, L. H. B. Nguyen, J. A. S. Oh, D. H. S. Tan, Y. S. Meng, Enabling a Co-Free, High-Voltage $LiNi_{0.5}Mn_{1.5}O_4$ Cathode in All-Solid-State Batteries with a Halide Electrolyte. *ACS Energy Lett*., 7, 2531–2539 (2022).

83. A. Cronk, Y. T. Chen, G. Deysher, S. Y. Ham, H. Yang, P. Ridley, B. Sayahpour, L. H. B. Nguyen, J. A. S. Oh, J. Jang, D. H. S. Tan, Y. S. Meng, Overcoming the Interfacial Challenges of $LiFePO_4$ in Inorganic All-Solid-State Batteries. *ACS Energy Lett.,* 8, 827–835 (2023).

84. Z. Lin, Z. Liu, W. Fu, N. J. Dudney, C. Liang, Lithium polysulfidophosphates: A family of lithium-conducting sulfur-rich compounds for lithium-sulfur batteries. *Angewandte Chemie - International Edition*, **52**, 7460–7463 (2013).

85. C. Zheng, K. Wang, L. Li, H. Huang, C. Liang, Y. Gan, X. He, W. Zhang, J. Zhang, High-Performance All-Solid-State Lithium–Sulfur Batteries Enabled by Slurry-Coated Li_6PS_5Cl/S/C Composite Electrodes. *Front Energy Res* **8**, (2021).

86. H. Pan. M. Zhang, Z. Cheng, H. Jiang, J. Yang, P. Wang, P. He, H. Zhou*,* Carbon-Free and Binder-Free Li-Al Alloy Anode Enabling an All-Solid-State Li-S Battery with High Energy and Stability. *Sci. Adv,* 8, 4372 (2022).

87. X. Gao, X. Zheng, Y. Tsao, P. Zhang, X. Xiao, Y. Ye, J. Li, Y. Yang, R. Xu, Z. Bao, Y. Cui*,* All-Solid-State Lithium-Sulfur Batteries Enhanced by Redox Mediators. *J Am Chem Soc* **143**, 18188–18195 (2021).

88. S. Ohno, R. Koerver, G. Dewald, C. Rosenbach, P. Titscher, D. Steckermeier, A. Kwade, J. Janek, W. G. Zeier, Observation of Chemomechanical Failure and the Influence of Cutoff Potentials in All-Solid-State Li-S Batteries. *Chemistry of Materials*, **31**, 2930–2940 (2019).

89. R. Schlem, C. F. Burmeister, P. Michalowski, S. Ohno, G. F. Dewald, A. Kwade, W. G. Zeier, Energy Storage Materials for Solid-State Batteries: Design by Mechanochemistry. *Adv. Energy Mater*., **11**, 2101022 (2021).

90. J. T. Kim, S. Hu, Y. Zhong, C. Wang, H. Wu, D. Zhao, C. Wang, X. Sun, Y. Li, All-solid-state lithium–sulfur batteries through a reaction engineering lens. *Nature Chemical Engineering* **1**, 400–410 (2024).

91. F. Chen, P. Puente, Y. Zhang, S. Cao, X. Lu, Z. Yi, Q. Shen, J. Li, All-solid-state lithium-sulfur batteries assembled by composite polymer electrolyte and amorphous sulfur/rGO composite cathode. *Solid State Ion* **380**, (2022).

92. L. Lodovico, S. Milad Hosseini, A. Varzi, S. Passerini, Amorphous Lithium Sulfide as Lithium-Sulfur Battery Cathode with Low Activation Barrier. *Energy Technology* **7**, (2019).

93. L. Li, Z. Ma, Y. Li, Accurate determination of optimal sulfur content in mesoporous carbon hosts for high-capacity stable lithium-sulfur batteries. *Carbon*, **197**, 200–208 (2022).

94. A. T. Ward, Raman Spectroscopy of Sulfur, Sulfur-Selenium, and Sulfur-Arsenic Mixtures. *J Phys Chem*., **72**, 4133–4139 (1968).

95. R. Dominko, A. Vizintin, G. Aquilanti, L. Stievano, M. J. Helen, A. R. Munnangi, M. Fichtner, I. Arcon, Polysulfides Formation in Different Electrolytes from the Perspective of X-ray Absorption Spectroscopy. *J Electrochem. Soc.,* **165**, A5014–A5019 (2018).

96. M. Tachez, J.-P. Malugani, R. Mercier, G. Robert, Ionic Conductivity of and Phase Transition in Lithium Thiophosphate Li_3PS_4. *Solid State Ionics*, **14**, 181-185 (1984).

97. T. K. Schwietert, V. A. Arszelewska, C. Wang, C. Yu, A. Vasileiadis, N. J. J. de Klerk, J. Hageman, T. Hupfer, I. Kerkamm, Y. Xu, E. van der Maas, E. M. Kelder, S. Ganapathy, M. Wagemaker, Clarifying the relationship between redox activity and electrochemical stability in solid electrolytes. *Nat. Mater*., **19**, 428–435 (2020).

98. M. Cuisinier, P. E. Cabelguen, S. Evers, G. He, M. Kolbeck, A. Garsuch, T. Bolin, M. Balasubramanian, L. F. Nazar, Sulfur speciation in Li-S batteries determined by operando X-ray absorption spectroscopy. *Journal of Physical Chemistry Letters*, **4**, 3227–3232 (2013).

99. A. Manceau, K. L. Nagy, Quantitative analysis of sulfur functional groups in natural organic matter by XANES spectroscopy. *Geochim. Cosmochim. Acta*., **99**, 206–223 (2012).

100. A. L. Santhosha, L. Medenbach, J. R. Buchheim, P. Adelhelm, The Indium−Lithium Electrode in Solid-State Lithium-Ion Batteries: Phase Formation, Redox Potentials, and Interface Stability. *Batteries & Supercaps*, **2**, 524–529 (2019).

101. B. A. Mei, O. Munteshari, J. Lau, B. Dunn, L. Pilon, Physical Interpretations of Nyquist Plots for EDLC Electrodes and Devices. *Journal of Physical Chemistry C*, **122**, 194–206 (2018).

102. J. Gu, Z. Liang, J. Shi, Y. Yang, Electrochemo-Mechanical Stresses and Their Measurements in Sulfide-Based All-Solid-State Batteries: A Review. *Adv. Energy Mater.*, **13**, 2203153 (2023).

103. H. Zhong, Y. Su, R. Ma, Y. Luo, H. Lin, J. Gu, Z. Gong, Y. Yang, Nano-Scale Interface Engineering of Sulfur Cathode to Enable High-Performance All-Solid-State Li–S Batteries. *Adv Funct. Mater*., doi: 10.1002/adfm.202315925 (2024).

104. X. Ji, K. T. Lee, L. F. Nazar, A highly ordered nanostructured carbon-sulphur cathode for lithium-sulphur batteries. *Nat. Mater*., **8**, 500–506 (2009).

105. F. Han, J. Yue, X. Fan, T. Gao, C. Luo, Z. Ma, L. Suo, C. Wang, High-performance all-solid-state lithium-sulfur battery enabled by a mixed-conductive Li_2S nanocomposite. *Nano Lett*., **16**, 4521–4527 (2016).

106. A. Schiele, T. Hatsukade, B. B. Berkes, P. Hartmann, T. Brezesinski, J. Janek, High-Throughput in Situ Pressure Analysis of Lithium-Ion Batteries. *Anal. Chem*., **89**, 8122–8128 (2017).

107. Z. Deng, Z. Wang, I.-H. Chu, J. Luo, S. P. Ong, Elastic Properties of Alkali Superionic Conductor Electrolytes from First Principles Calculations. *J. Electrochem. Soc.*, **163**, A67–A74 (2016).

108. D. H. S. Tan, Y.-T. Chen, H. Yang, W. Bao, B. Sreenarayanan, J.-M. Doux, W. Li, B. Lu, S.-Y. Ham, B. Sayahpour, J. Scharf, E. A. Wu, G. Deysher, H. E. Han, J. Hah, H. Jeong, J. B. Lee, Z. Chen, Y. S. Meng, Carbon-free high-loading silicon anodes enabled by sulfide solid electrolytes. *Science* **373**, 1494–1499 (2021).

109. J. N. Reimers, J. R. Dahn, Electrochemical and In Situ X-Ray Diffraction Studies of Lithium Intercalation in Li_xCoO_2. *J. Electrochem. Soc.*, **139**, 2091–2097 (1992).

110. H. Huo, M. Jiang, Y. Bai, S. Ahmed, K. Volz, H. Hartmann, A. Henss, C. V. Singh, D. Raabe, J. Janek, Chemo-mechanical failure mechanisms of the silicon anode in solid-state batteries. *Nat. Mater.*, **23**, 543-551 (2024).

111. R. Koerver, W. Zhang, L. De Biasi, S. Schweidler, A. O. Kondrakov, S. Kolling, T. Brezesinski, P. Hartmann, W. G. Zeier, J. Janek, Chemo-mechanical expansion of lithium electrode materials-on the route to mechanically optimized all-solid-state batteries. *Energy Environ. Sci.,* **11**, 2142–2158 (2018).

112. D. H. S. Tan, Y. S. Meng, J. Jang, Scaling up high-energy-density sulfidic solid-state batteries: A lab-to-pilot perspective. *Joule*, **6,** 1755-1769 (2022).

113. Y. G. Lee, S. Fujiki, C. Jung, N. Suzuki, N. Yashiro, R. Omoda, D. S. Ko, T. Shiratsuchi, T. Sugimoto, S. Ryu, J. H. Ku, T. Watanabe, Y. Park, Y. Aihara, D. Im, I. T. Han, High-energy long-cycling all-solid-state lithium metal batteries enabled by silver–carbon composite anodes. *Nat Energy,* **5**, 299–308 (2020).

114. S. Y. Ham, E. Sebti, A. Cronk, T. Pennebaker, G. Deysher, Y. T. Chen, J. A. S. Oh, J. B. Lee, M. S. Song, P. Ridley, D. H. S. Tan, R. J. Clément, J. Jang, Y. S. Meng, Overcoming low initial coulombic efficiencies of Si anodes through prelithiation in all-solid-state batteries. *Nat. Commun.,* **15** (2024).

115. B. Ravel, M. Newville, ATHENA, ARTEMIS, HEPHAESTUS: Data analysis for X-ray absorption spectroscopy using IFEFFIT. *Journal of Synchrotron Radiation,* **12**, 537–541 (2005).

116. M. Duquesnoy, T. Lombardo, M. Chouchane, E. N. Primo, A. A. Franco, Data-driven assessment of electrode calendering process by combining experimental results, in silico mesostructures generation and machine learning. *J Power Sources,* **480** (2020).

117. S. J. Cooper, A. Bertei, P. R. Shearing, J. A. Kilner, N. P. Brandon, TauFactor: An open-source application for calculating tortuosity factors from tomographic data. *SoftwareX,* **5**, 203–210 (2016).

118. A. P. Tran, S. Yan, Q. Fang, Improving model-based functional near-infrared spectroscopy analysis using mesh-based anatomical and light-transport models. *Neurophotonics,* **7**, 1 (2020).

119. G. Wang, L. Ketter, T. Zhao, E. Nazmutdinova, M. Kraft, W. Zeier, High Areal Capacity Cation and Anionic Redox Solid-State Batteries Enabled by Transition Metal Sulfide Conversion. ACS Applied Materials and Interfaces, 16, 42189-42197 (2024).

120. T. Yu, H. Li, Y. Liu, J. Li, J. Tian, Z. Liu, Y. Rao, S. Guo, H. Zhou. A Prototype of Dual-Ion Conductor for All-Solid-State Lithium Batteries. Sci. Adv. 9, eadj8171 (2023).

121. Y. Chen, J. Jang, J.A.O. Sam, S.-Y. Ham, H. Yang, D.-J. Lee, M. Vicencio, J. B. Lee, D. H.S. Tan, M. Chouchane, A. Cronk, M.-S. Song, Y. Yin, J. Qian, Z. Chen, Y.S. Meng. Enabling Uniform and Accurate Control of Cycling Pressure for All-Solid-State Batteries. Adv. Energy Mater. 14, 2304327 (2024).